A Numerical Investigation of Subsonic and Supersonic Flow Around Axisymmetric Bodies

by George D. Catalano and Walter B. Sturek, Sr.

20020130 052

Army Research Laboratory

A Numerical Investigation of Subsonic and Supersonic Flow Around Axisymmetric Bodies

George D. Catalano
U.S. Military Academy

Walter B. Sturek, Sr.
Computational and Information Sciences Directorate, ARL

Abstract

A computational fluid dynamics (CFD) approach to predicting high-speed aerodynamic flow fields of interest to the U.S. Army Research Laboratory (ARL) has been carried out. The aerodynamic problems of particular interest are (1) supersonic flow past the aftbody of projectiles with base mass injection, (2) supersonic flow past the M549 projectile, and (3) subsonic, transonic, and supersonic flow past an M864 projectile with base bleed and wake combustion.

The commercially available FLUENT (Fluent, Inc. *FLUENT*. Version 5.1.1, Lebanon, NH, 1999.) CFD code was utilized. The computational effort supports an ongoing ARL-sponsored experimental investigation. Of particular interest in the present investigation is the careful characterization of the various turbulence models employed in the CFD code. Additionally, the ease of use and set-up as well as the computational time will be described.

An experimental effort (Dutton, J. C., and A. L. Addy. "Fluid Dynamic Mechanisms and Interactions Within Separated Flows." U.S. Army Research Office Research Grant DAAH04-93-G-0226 and the Department of Mechanical and Industrial Engineering, University of Illinois, Urbana-Champagne, Urbana, IL, August 1998.) consisting of detailed laser Doppler velocimeter (LDV), particle image velocimeter (PIV), and high-speed wall pressure measurements has been made in axisymmetric and planar subsonic and supersonic flows with embedded separated regions. The present work seeks to predict similar flow fields computationally and to address areas of agreement and disagreement.

Contents

INTENTIONALLY LEFT BLANK.

List of Figures

INTENTIONALLY LEFT BLANK.

List of Tables

INTENTIONALLY LEFT BLANK.

1. Introduction

A computational fluid dynamics (CFD) approach to predicting high-speed aerodynamic flow fields of interest to the U.S. Army Research Laboratory (ARL) has been carried out. The aerodynamic problems of particular interest are supersonic flow past the aftbody of projectiles with base mass injection and supersonic flow past the M549 projectile.

The commercially available FLUENT [1] CFD code was utilized. The computational effort supports an ongoing ARL-sponsored experimental investigation. Of particular interest in the present investigation is the careful characterization of the various turbulence models employed in the CFD code. Additionally, the ease of use and set-up as well as the computational time will be described.

Previous computational studies of base flow for transonic and supersonic free stream velocities carried out at ARL using Navier-Stokes techniques are reported in references [2–4]. Sahu and Heavey [3] compared the results of their computational study to experimental data and found the standard k-epsilon (k-ε) turbulence model performed better in the wake region than an algebraic model.

An experimental effort [5] consisting of detailed laser Doppler velocimeter (LDV), particle image velocimeter (PIV), and high-speed wall pressure measurements has been made in axisymmetric and planar subsonic and supersonic flows with embedded separated regions. The work concentrated, in part, on the following key issues:

- supersonic base flow in the near wake of a cylindrical afterbody,
- supersonic near-wake afterbody boattailing effects on axisymmetric bodies,
- effects of rapid expansion on the development of compressible free shear layers,
- subsonic base cavity flow-field structure,
- base bleed with a cylindrical afterbody in supersonic flow,
- turbulent structures in a supersonic base flow with base bleed,
- turbulence structure of reattaching axisymmetric free shear layers, and
- shock-separated free shear layers.

The present work seeks to predict similar flow fields computationally and to address areas of agreement and disagreement.

2. Supersonic Flow Past an Aftbody

2.1 Experimental Flow Field

The flow field investigated is a blunt cylindrical body with base bleed aligned in a supersonic flow (Figure 1). The supersonic free stream expands as it turns the corner while the turbulent boundary layer separates and then undergoes recompression, realignment, and redevelopment in the wake of the underbody [5]. Fluid from the region adjacent to the base is entrained and accelerated by the outer shear layer and then returned to the base region by a recompression shock system. This region is referred to as the primary recirculation region. Introducing base bleed, the primary recirculation region is moved downstream from the aftbody with a forward stagnation point created, dependent on the relative strengths of the bleed jet and the recirculating region. Experiments performed by several investigators (see reference [5] for a complete list) have demonstrated the important effect of such a shift in the location of the primary recirculation region—a change in the base pressure ratio and, as a result, a change in the aftbody drag. Base bleed then is an effective mechanism for reducing aftbody drag.

The experimental flow conditions and geometry are listed in Table 1.

2.2 Computational Grid

Gambit [6], a single integrated preprocessor for CFD analysis, was used for geometry construction and import. In addition, Gambit, used for mesh generation, has the capability to produce structured and unstructured hexahedral, tetrahedral, pyramid, and prism computational cells. Mesh quality examination as well as boundary zone assignment capability is also provided. The general sequence of operation for Gambit's use includes the following steps:

- initial setup including solver selection, mesh size, etc.,
- geometry creation,
- meshing including edge and boundary layer meshing followed by face and/or volume meshing,
- mesh examination,
- zone assignment, and
- mesh export.

2

For the present investigation, the flow field is modeled as axisymmetric flow past a cylindrical aftbody with no swirl. Thus, the generation of suitable grid geometry was straightforward. An appropriate length of the cylinder embedded in the flow field was calculated using boundary layer theory corresponding to existing experimental data. For all grids generated in the present work, a length of cylinder equal to 0.14 m was chosen.

An important aspect of the present work was to determine the effect of mesh density on the calculated results. For the grid face size area of 0.4 m × 0.6 m, the number of cells varied from a low of approximately 7000 to a maximum of nearly 64,000, thus affording an order of magnitude difference in this potentially important parameter.

The actual grids used in this investigation are shown in Figure 2. Modifications to the simple cylindrical grid were incorporated in order to model a cylindrical boattail mounted behind the cylinder. The boattail grid geometry is presented in Figure 3 and is based on the experimental prototype of Herrin and Dutton [7]. The boattail chosen for this experimental investigation has a conical shape with an angle relative to the horizontal of 5° and length 31.75 mm (0.5 cal.). Reid and Hastings [8] have shown that the optimal boattail shape is essentially conical at moderate supersonic speeds for typical boattail lengths. The 5° angle has also been shown to be near the optimal angle from previous investigations [8].

2.3 Computational Models

Three different turbulence models [9] are used in the present investigation: (1) the Spalart-Allmaras one-equation model, (2) the standard k-ε two-equation model, and (3) the Reynolds stress five-equation model (Table 2).

In turbulence models that employ the Boussinesq approach, the central issue is how the eddy viscosity is computed. The model proposed by Spalart and Allmaras solves a transport equation for a quantity that is a modified form of the turbulent kinematic viscosity.

The standard k-ε model is a semi-empirical model based on model transport equations for the turbulent kinetic energy (k) and its dissipation rate (ε). The model transport equation for k is derived from the exact equation, while the model transport equation for ε was obtained using physical reasoning and bears little resemblance to its mathematically exact counterpart.

In the derivation of the k-ε model, it was assumed that the flow is fully turbulent, and the effects of molecular viscosity are negligible. The standard k-ε model is therefore valid only for fully turbulent flows.

The Reynolds stress model (RSM) is the most elaborate turbulence model that FLUENT [1] provides. Abandoning the isotropic eddy-viscosity hypothesis, the RSM closes the Reynolds-averaged Navier-Stokes equations by solving transport

equations for the Reynolds stresses, together with an equation for the dissipation rate. This means that four additional transport equations are required in two-dimensional (2-D) flows, and seven additional transport equations must be solved in three-dimension (3-D).

2.4 Comparison With Varying Grid Densities

Results are described for various flow field properties with the turbulence closure model kept constant but with the grid density or number of cells within the grid volume varying. The turbulence models and the corresponding number of cells are listed in Table 3.

In this report, numerical results for the RSM are presented. Streamwise mean velocity contours are presented in Figure 4 and the turbulent kinetic energy contours are shown in Figure 5. These results are for a mass bleed ratio equal to 0.01. For the case of the streamwise velocity, the contours are nearly identical for the approximate order-of-magnitude difference in grid density. The results are quite different for the turbulent kinetic energy contours, particularly near the base of the aftbody. The region of relatively low turbulent kinetic energy extends much farther downstream from the base region indicating a much diminished momentum mixing or transport occurring from the outer free stream towards the wake.

Though not included here, results for the streamwise mean velocity contours for both the Spalart-Allmaras and standard k-ε models behaved similarly. That is, the contours remained nearly identical from coarsest to finest grid density.

2.5 Comparison With Varying Turbulence Models

In order to compare the results for the varying turbulence closure models, contour plots of streamwise mean velocities are presented. The profiles are shown for the finest grid density.

In Figure 6, the steamwise velocity contours are compared for two closure models. Note that a similar observation can be made about the region near the base as was made for the turbulent field for the case of varying grid density. The more detailed and presumably higher order model, the RSM, tends to show an elongated wake region near the base as compared to the Spalart-Allmaras model. Thus, increasing the complexity of the model seems to result in the same effect as increasing the grid cell density. Though not shown here, the radial velocity gradient is greatest for the case of the Spalart-Allmaras model (i.e., the lowest order model) and least for the RSM (i.e., highest order model). Similarly, static pressure contours exhibit higher gradients for the Spalart-Allmaras models as compared to the RSM.

4

2.6 Comparison With Experimental Data

Comparisons are made with experimental data for supersonic flow past a cylindrical aftbody without base bleed, with base bleed, and for a cylindrical aftbody plus boattail with and without base bleed [5]. For all the comparisons shown, the Reynolds stress turbulence closure model is used as well as the finest cell density. For the cases involving base bleed, the flow exits the cylindrical aftbody parallel to the free stream direction with the base bleed mass injection rate equal to 0.01 times the mass flux injection rate if the entire base area served as the exit area for the nozzle. The velocity of the base bleed is considered to be constant over the exit plane.

2.6.1 No Base Bleed (I = 0.00)

In Figure 7, streamwise mean velocity profiles are presented for the case of zero base bleed [5]. The non-dimensionalized streamwise velocity, U/U_{fs}, is plotted vs. non-dimensionalized radial location, r/R, for three downstream locations, x/D = 1.26, 1.42, and 1.73. The numerical results are compared to the experimental data. The agreement is quite good but with the numerical model consistently overestimating the extent of the mean wake region and thus overestimating the magnitude of the mean, axial velocity gradient.

In Figure 8, non-dimensionalized turbulent shear stress ($-uv/U_{fs}^2$) profiles are presented at the same downstream locations (x/D = 1.26, 1.42, and 1.73). The numerical results underestimate the maximum value of the turbulent stress and underestimate the extent of the turbulent velocity field as compared to experimental data. This is in direct contrast to the results for the mean velocity field.

In Figure 9, the base pressure (here nondimensionalized by free stream static pressure) distribution is compared to experimental results. Averaging over the length of the base, the pressure ratios are nearly identical.

2.6.2 Base Bleed (I = 0.01)

In Figure 10, streamwise mean velocity profiles are shown for four downstream locations (x/D = 0.95, 1.26, 1.95, 2.04). The results are much closer to the actual experimental data [8] suggesting that the numerical model more accurately predicts the important flow features in the case of base bleed.

In Figure 11, radial mean velocity profiles are presented for x/D = 0.95, 1.26, 1.95, and 2.04. The agreement with experimental data is not as good as is the case for the streamwise velocity data. Consistently, the numerical data overestimates the magnitude of the radial mean velocity at each downstream location. This would indicate there is more turning in the flow field numerically than measured experimentally.

In Figure 12, the turbulent kinetic energy profiles ($1/2\,[u^2 + v^2 + w^2]^{1/2}$) at the downstream locations x/D = 0.95, 1.26, 1.95, and 2.04 are presented. The agreement both in magnitude of the turbulent kinetic energy and in location is quite good.

In Figure 13, the turbulent stress, $-uv/Ufs^{\wedge}2$, profiles at x/D = 0.95, 1.26, 1.95, and 2.04 also demonstrate excellent agreement with the experimental data.

In Figure 14, the downstream development of the axial mean velocity is presented. The magnitudes are in quite close agreement with the experimental data as is the location of the zero velocity or leading edge of the recirculation region.

In Figure 15, the base pressure, Pb/Pfs, is shown for the region outside the base bleed exit with the agreement with experimental data quite good.

2.6.3 Aftbody Boattail Without and With Base Bleed (I = 0.00 and I = 0.01)

Axial mean velocity, U/Ufs, and turbulent kinetic energy, $k/Ufs^{\wedge}2$, as a function of downstream location are shown in Figures 16 and 17, respectively, for the no bleed and bleed cases [5]. Agreement is quite good throughout the range of downstream locations though does improve with distance from the exit plane. This is especially true downstream of the leading edge of the recirculation region.

---

3. Supersonic Flow Past M549 Projectile

A series of computations have been performed for the M549 configuration shown in Figure 18. This portion of the present investigation was performed in order to gain experience using the grid generation technique for a more complicated geometry than the previously investigated flow past an aftbody. The Mach number was set equal to 2.47 for all computations at zero angle of attack. The computational flow conditions and geometry are listed in Table 4.

Qualitative features of the computed flow fields are presented in the form of contours of the axial and radial mean velocity fields, and contours of the turbulent kinetic energy and uv-Reynolds stress.

The grid geometry for the flow past the M549 projectile (not shown) was obtained using the grid-adaption feature of the FLUENT [1] code to obtain a higher density of cells in region of high static pressure gradient. No experimental data are available for comparison so only numerical results are provided.

Contours for the axial velocity and radial mean velocities are presented in Figures 18 and 19. In Figure 20, the contour plot for the mean static pressure field is shown. The turbulent velocity field is detailed with contour plots of the turbulent kinetic energy and the Reynolds shear stress in Figures 21 and 22, respectively.

6

The axial mean velocity contours shown in Figure 18 demonstrate the important characteristics of the flow field. The flow first encounters a compression region near the nose of the projectile, followed by a weaker compression at the waist, and then subsequently followed by a turbulent wake region at the base. Evidence of the turbulent boundary layer growth along the length of the projectile is evident. The radial mean velocity contours presented in Figure 19 indicate the existence of strong recirculation behind the base region and large influx of the outer free stream flow. The mean static pressure contours (Figure 20) reinforce the earlier observations concerning the existence of compression regions near the nose, near the waist, and in the wake region behind the base.

The turbulent flow field contours presented in Figures 21 and 22 add further to an understanding of the resultant flow. The uv-component of the Reynolds stress is selected as it provides the greatest insight into the origin of the turbulence. Note that the regions of highest turbulent kinetic energy correspond to regions of relatively low magnitude of the shear stress term. Conversely, the maximum values for the shear stress occur immediately behind the base where the turbulent kinetic energy remains at a low level. Thus, the turbulent flow field begins to develop or is generated close to the base and then, as the flow convects downstream, reaches a maximum before being attenuated by the effect of the viscosity of the fluid.

4. Subsonic and Supersonic Flow Past M864 Projectile

The M864 is an Army shell that burns a solid propellant that exhausts into the base region to achieve reduced aerodynamic drag. It is a 155-mm, extended range, cargo-carrying projectile. A schematic of the M864 is shown in Figure 23. Note that the boattailed section includes a domed cavity and a combustion chamber for the solid propellant. The products of the combustion exit through an orifice plate rather than a traditional DeLaval (C-D) nozzle, as the M864 is considered to be of base bleed design rather than a rocket-assisted projectile.

An initial numerical investigation by Nietubicz and Gibeling [10] modeled the solid propellant combustion using the approach developed by Giebling and Buggeln [11]. This study [10] modeled the combustion as injectant gas mixtures of H_2 and H_2/CO for a base bleed ratio of $I = 0.0022$. These combustion results were compared to results for hot air bleed and zero bleed conditions. The computations were carried out for $M = 2.0$ and zero angle of attack. The results indicated that the effect of the hot mass injection was confined to a region very near the base, whereas the combustion products affected a much wider region of the base region flow field.

4.1 Wake Combustion Model

The present numerical investigation of the M864 includes the effects of the inclusion of the domed cavity, the injection of high temperature fluid at the base exit plane and the effect of wake combustion. The wake combustion has been incorporated into the calculation based upon the published FLUENT [1] tutorial for nozzle flow for a solid-propellant rocket. A brief description of this model is now provided.

The mass flow of the solid propellant exiting a nozzle, or, in the present case, an orifice, is given by:

$$I = \partial r / \partial t * A \, \rho b = \eta * [Pc] \uparrow N, \tag{1}$$

where,

$\partial r / \partial t$ = surface burning rate,

A = base area,

ρb = density of solid propellant,

η = empirically determined constant,

Pc = fluid pressure in the combustion chamber, and

N = empirically determined constant.

For the present work, the mass flow rate was set at 0.01, and then the empirical constants were calculated at the appropriate flow conditions to obtain this mass flow rate.

Computations have been carried out for the case of zero angle of attack for a free stream Mach number range of 0.8–3.0 (Table 5). Qualitative features of the computed flow fields are presented in the contours of the axial and radial mean velocity fields, contours of the turbulent kinetic energy and uv-Reynolds stress, and contours of the mean static temperature fields. Quantitative descriptions of the various flow fields are also provided including the downstream or streamwise development of the mean velocity distributions.

For the present investigation, the RSM for turbulence was used exclusively. This particular turbulence model was chosen based on the earlier work of the principal investigator focusing on the simpler aftbody geometry, and the M549 projectile.

4.2 Discussion of Results

Contours for the axial mean velocity fields for the three Mach numbers with base bleed and both with and without wake combustion are presented in Figures 24–26. For a given mass bleed, increasing the free stream Mach number increases the turning of the flow around the base exit plane. This is similar to the

8

effect of increasing the relative velocity differences in mixing layers and in coaxial jets. Greater mean velocity ratios serve to increase the mixing more rapidly.

Contours for the radial mean velocity fields for the supersonic Mach numbers with base bleed and both with and without wake combustion are presented in Figures 27 and 28. Increasing the velocity ratio pulls the standing vortex located near the base region toward the rear of the projectile. The wake combustion in turn flattens the vortex and tends to diffuse or flatten the area of steepest radial velocity gradient toward the outer reaches of the base region.

Contours for the turbulent kinetic energy fields for the three Mach numbers with base bleed and both with and without wake combustion are presented in Figures 29–31. The presence of wake combustion seems to aid in the transfer of the flow energy from the mean velocity field to the turbulent velocity field. That is, the regions of highest turbulent kinetic energy have convected downstream more rapidly with the inclusion of the wake combustion. However, it is worth noting that the high supersonic case seems to be least affected.

Contours for the turbulent uv-Reynolds shear stress fields for the three Mach numbers with base bleed and both with and without wake combustion are presented in Figures 32–34. Increasing the free stream Mach number tends to increase the magnitude of the uv component of the Reynolds shear stress and pull that region of maximum value closer to the base. Similarly, the introduction of wake combustion also increases the magnitude of the uv component of Reynolds stress and pull regions of highest gradient toward the base.

In Figures 35–38, contour plots for M=3.0 and with wake combustion are presented. The contour plots indicate the important features of the resultant flow field and are not provided as a summary of the computational results.

5. Summary

Computations have been performed for flow past an aftbody, an aftbody with boattailing, and the M549 projectile configuration.

A numerical investigation has been made for supersonic flow past a cylindrical aftbody with and without base bleed and with and without a cylindrical boattail. The effects of grid cell density and turbulence model were each examined. The computational fluid dynamics software FLUENT [1] Version 5.1.1 was used for all calculations. The presentation of the graphs extensively used Adobe Illustrator Version 7.0. The mean and turbulent velocity and pressure fields all were documented.
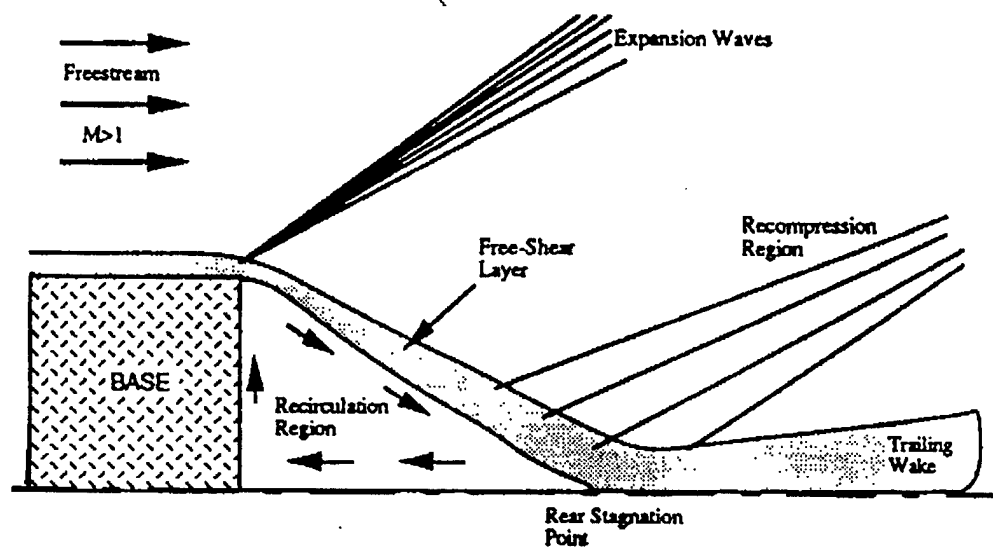
The grid density was found to have its most significant effect on the calculations of the turbulent velocity field while the mean velocity field was essentially independent of grid cell density.

Three different turbulent models were employed in the present investigation, the Spalart-Allmaras one-equation model, the standard k-ε two-equation, model and the Reynolds stress five-equation model. The more detailed and presumably higher order model, the RSM, tends to show an elongated wake region near the base as compared to the other two models. Increasing the complexity of the model seems to result in the same effect as increasing the grid cell density.

The numerical calculations were found to be closest to the experimental data for the case of mass base bleed than in the case of no mass base bleed. The presence or absence of the aft boattail did not seem to have an effect on the comparison of numerical and experimental data.

For the flow past the M549 projectile, the mean and turbulent velocity fields were described with experience gained in modeling flows past finite bodies of revolution. Before this portion of the investigation, only sections of the projectile, the aftbody, were investigated numerically.

Computations for the reacting M864 base bleed projectile provided results for the effect of temperature on the base region standoff distance that were not fully consistent with previous results of Nietubicz [10], which modeled the combustion process as a finite-rate reacting gas mixture. However, there are significant differences in the two approaches with respect to the combustion model, base bleed mass rate, numerical scheme, and turbulence model. Additional effort is required to identify the source of the discrepancies and establish the optimum modeling technique for this complex flow field.

10

Expansion Waves

Freestream

M>1

Recompression
Region

Free-Shear
Layer

BASE

Recirculation
Region

Trailing
Wake

Rear Stagnation
Point

Courtesy of Dr. Craig Dutton [5]

Figure 1. Schematic diagram of supersonic base flow.
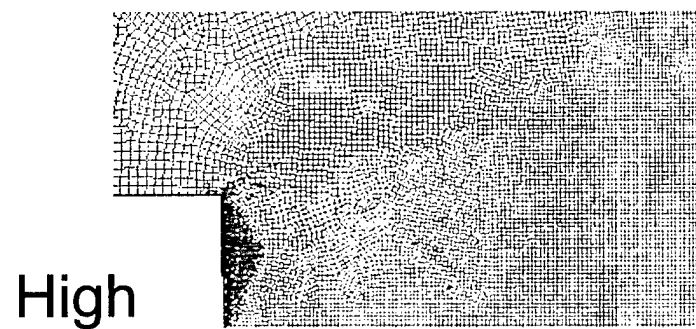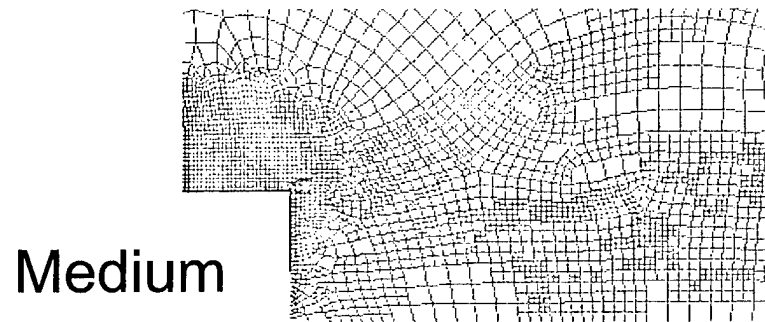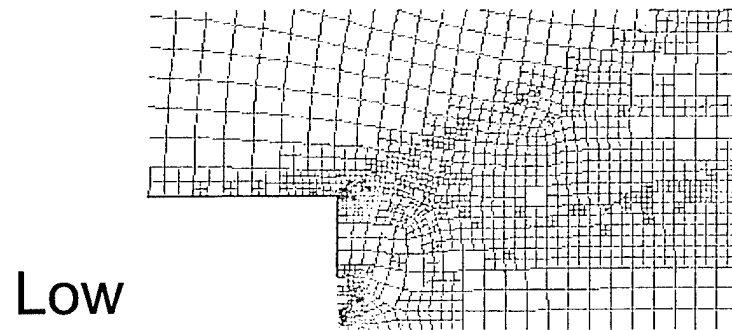
Low

Medium

High

Figure 2. Grid geometry and variation of grid densities for flow past aftbody.

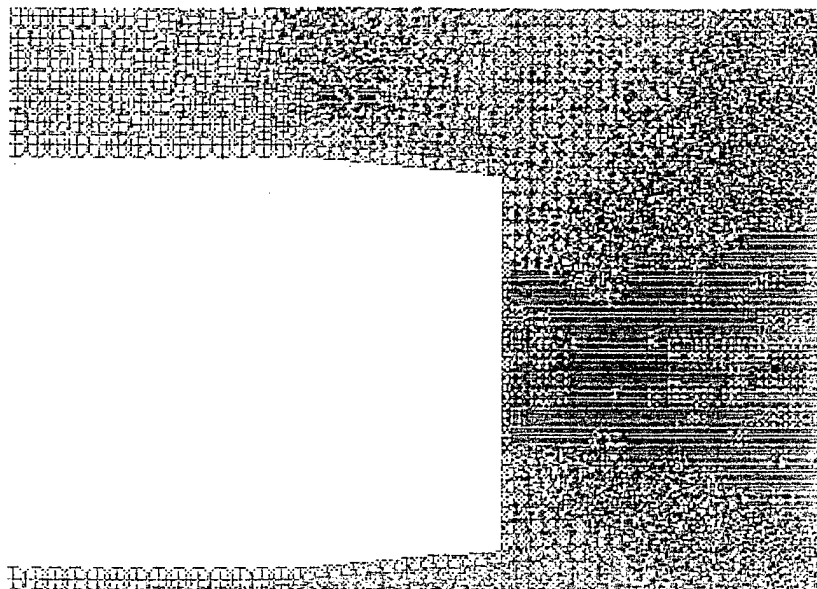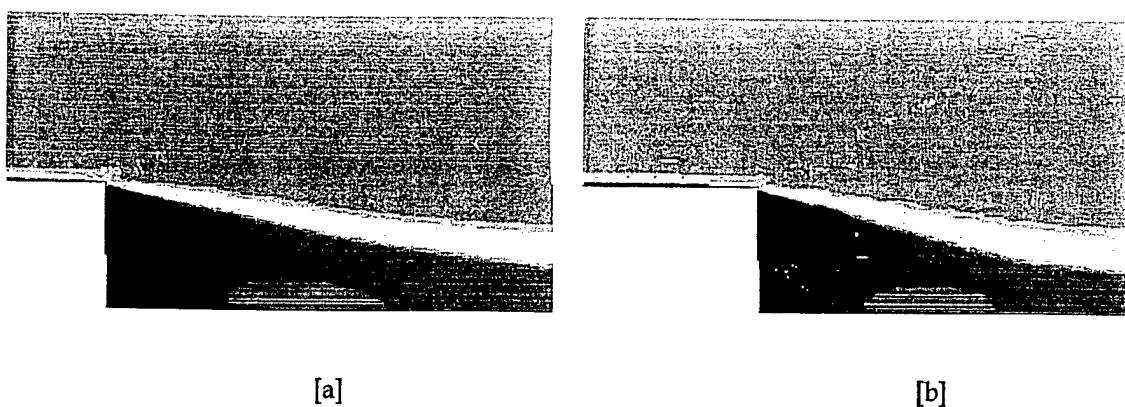Figure 3. Grid geometry for flow past aftbody with boattail.

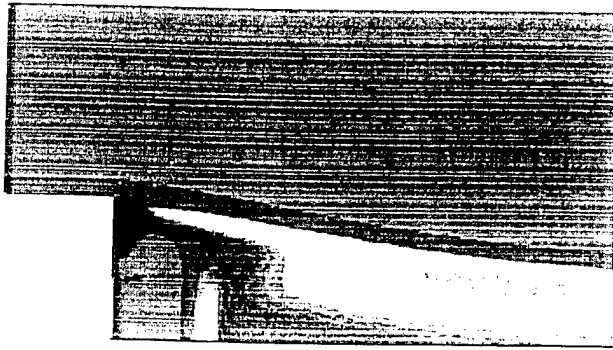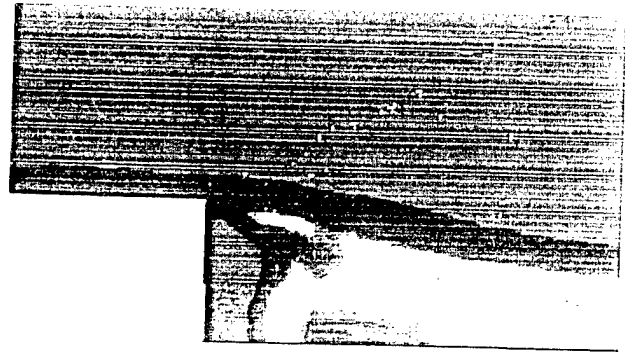[a]   [b]

Figure 4. Comparison of streamwise mean velocity contours for high and low grid number densities ([a] high grid number density = 64k vs. [b] low grid number density = 9k).

[a]   [b]

Figure 5. Comparison of turbulent kinetic energy contours for high and low grid number densities ([a] high grid number density = 64k vs. [b] low grid number density = 9k).
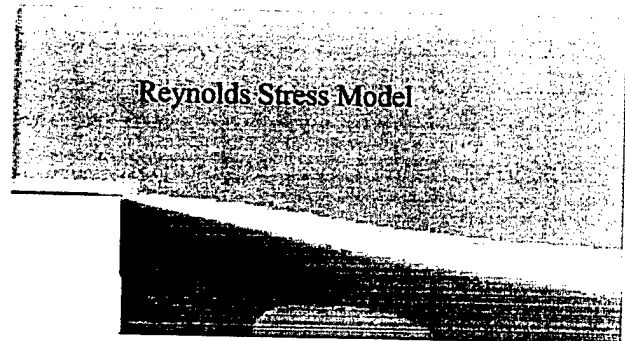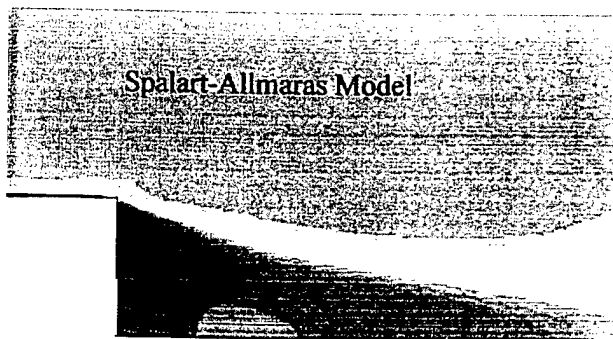

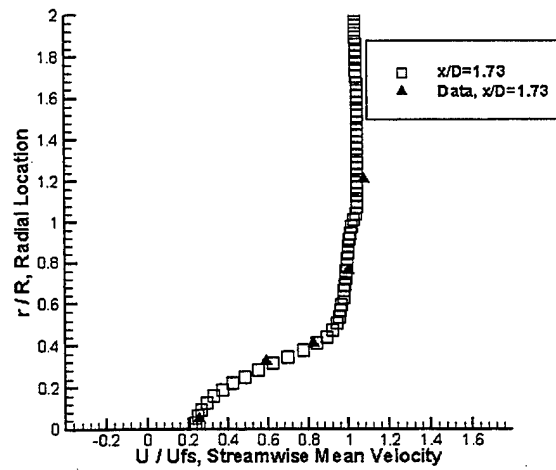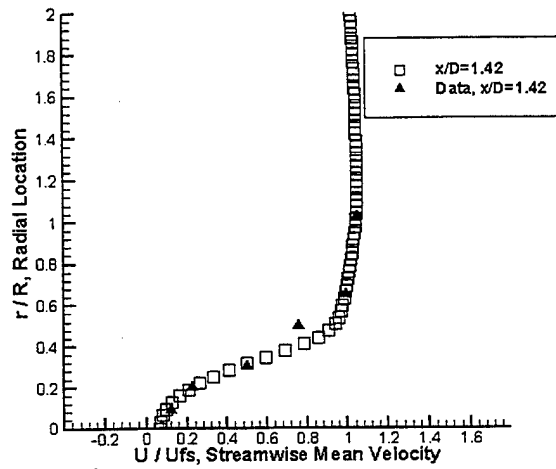Figure 6. Comparison of streamwise mean velocity contours for varying turbulence models.

14

Figure 7. Streamwise mean velocity (U/Ufs) profiles as a function of radial position (r/R) for various downstream locations (compared to experimental data) for no base bleed (I = 0.0).

Figure 8. Turbulent shear stress (-uv/Ufs^2) as a function of radial position (r/R) for various downstream locations (compared to experimental data) for no base bleed (I = 0.0).

Figure 9. Non-dimensionalized base pressure distribution, Pb/Pfs, vs. radial location on base for no base bleed (I = 0.0) with comparison to experimental data.
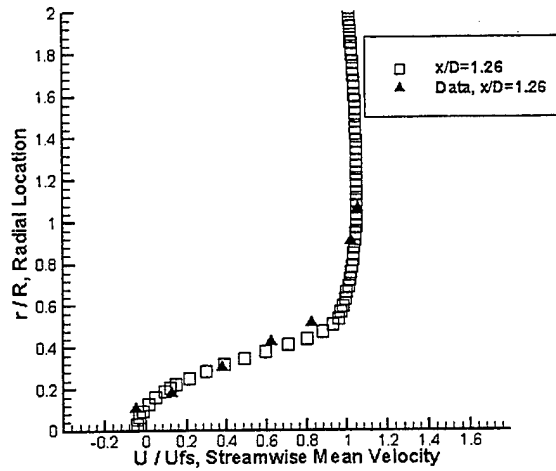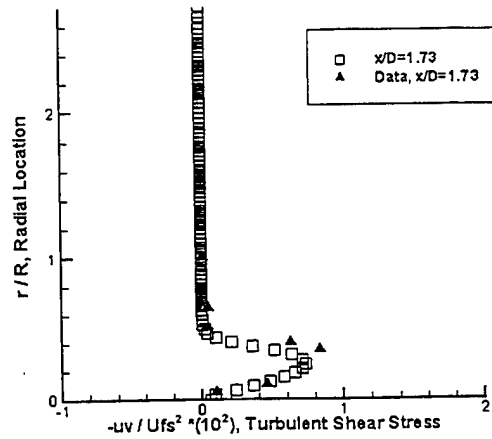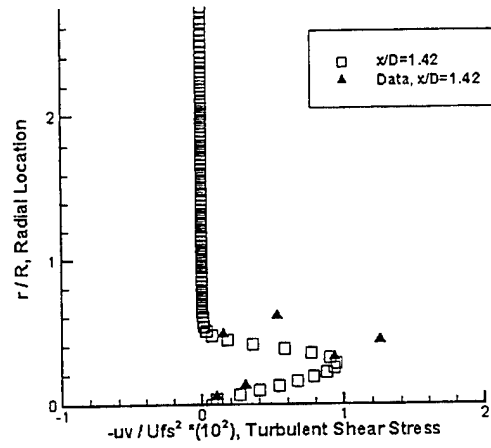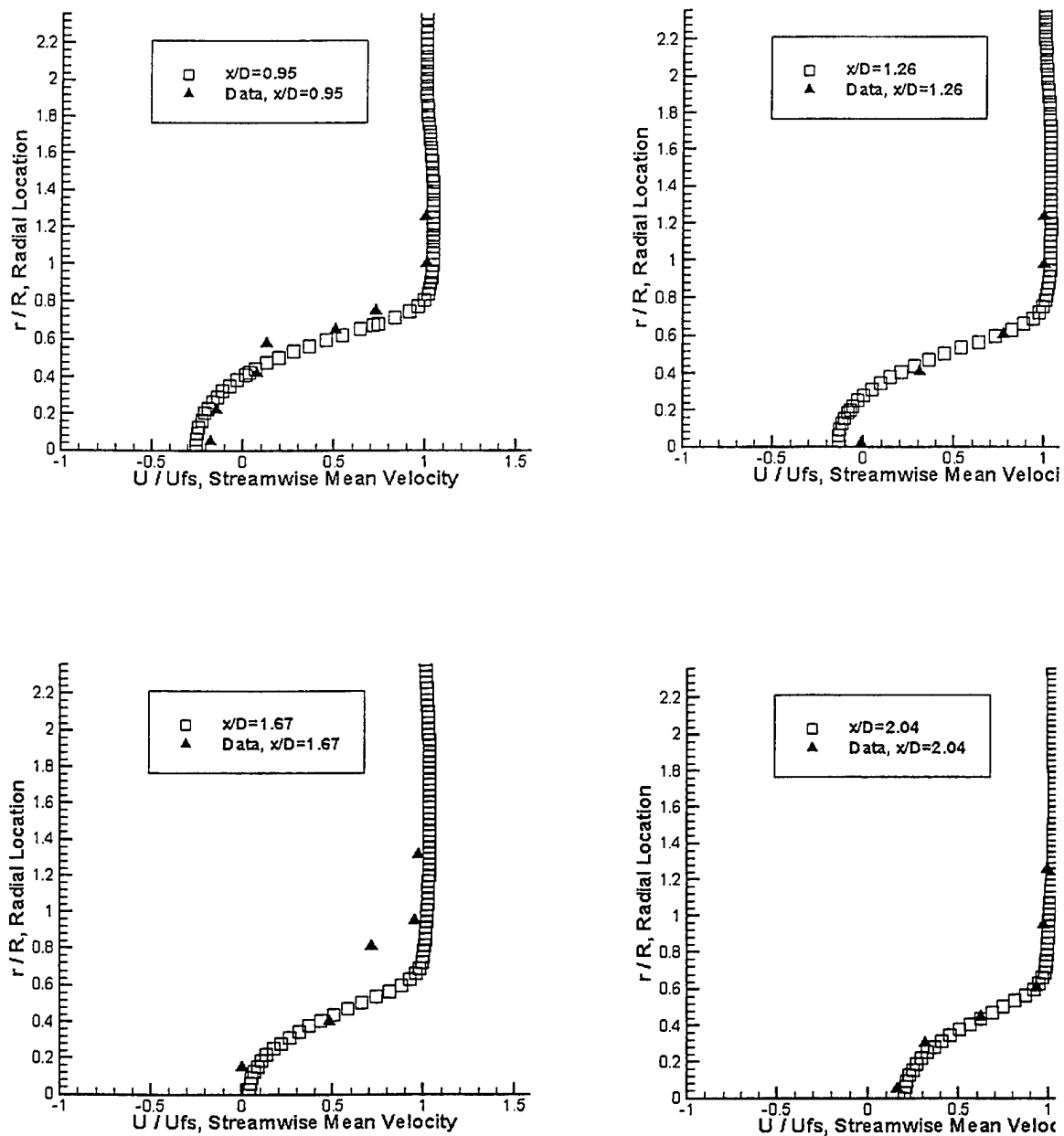
Figure 10. Streamwise mean velocity (U/Ufs) profiles as a function of radial position (r/R) for various downstream locations (compared to experimental data) for base bleed (I = 0.01).
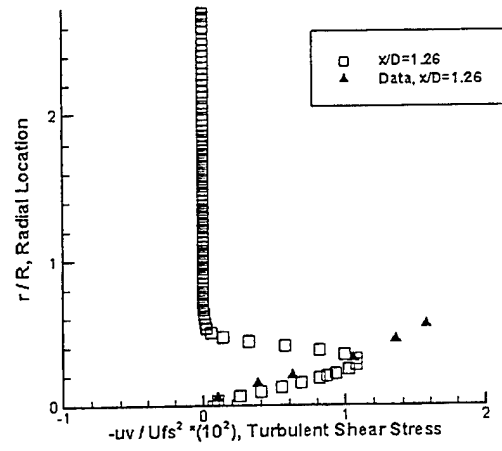
18

Figure 11. Radial mean velocity (V/Ufs) as a function of radial position (r/R) for various downstream locations (compared to experimental data) for base bleed (I = 0.01).

19
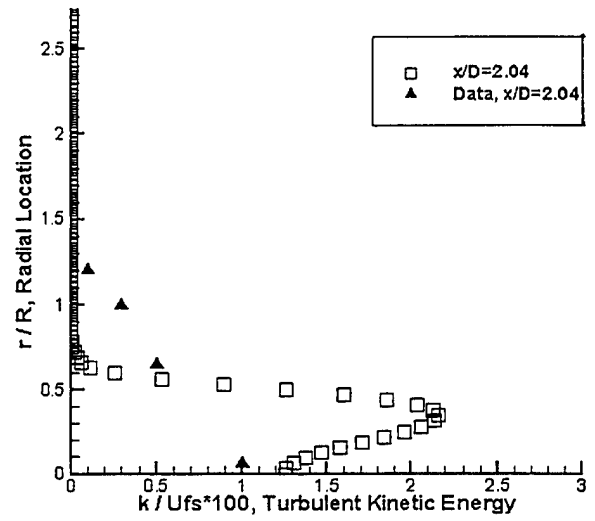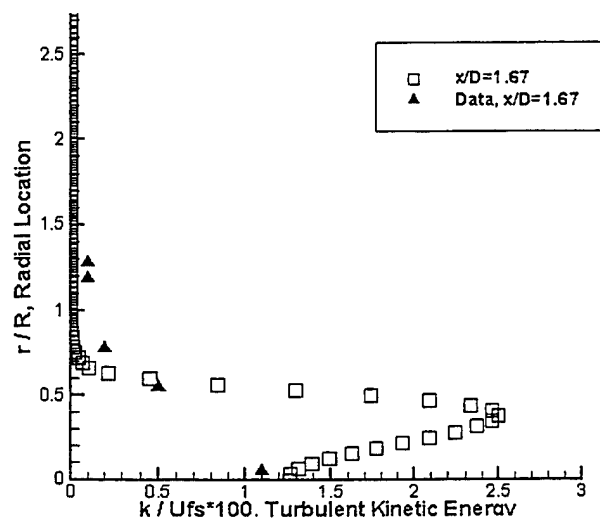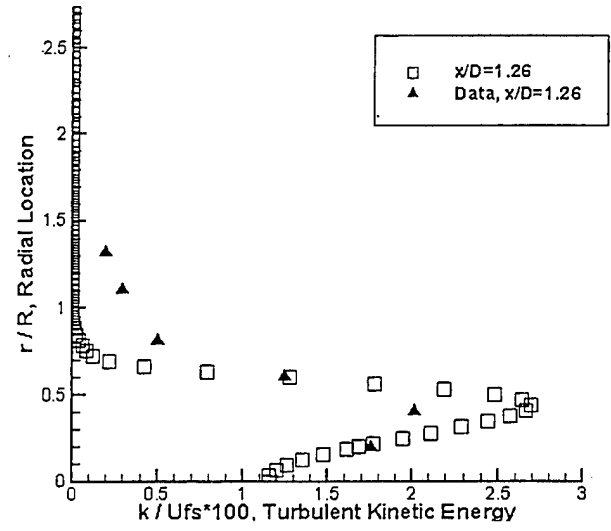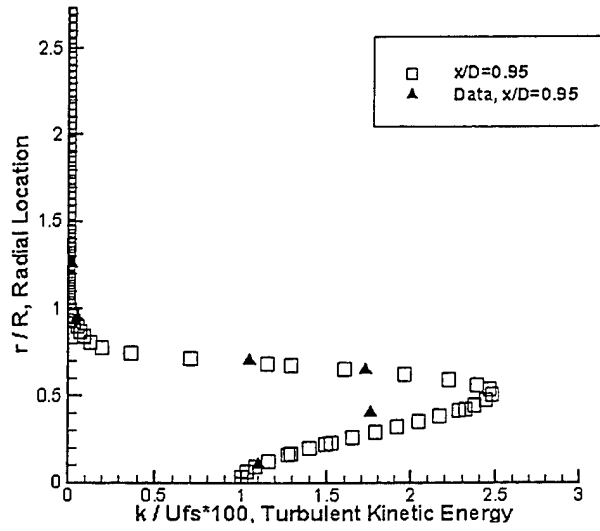
Figure 12. Turbulent kinetic energy (k/Ufs^2) as a function of radial position (r/R) for various downstream locations (compared to experimental data) for base bleed (I = 0.01).
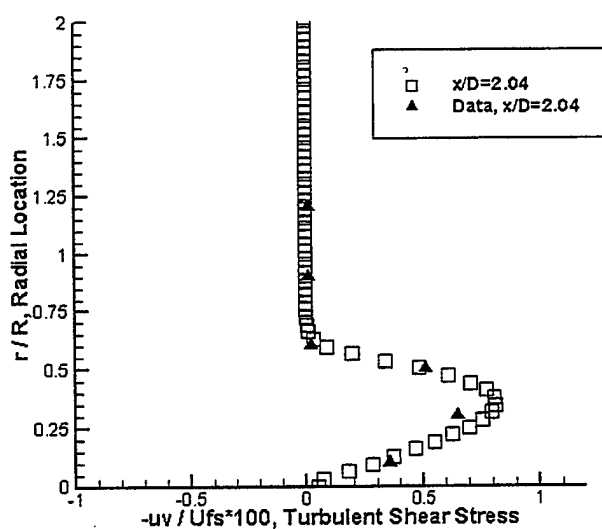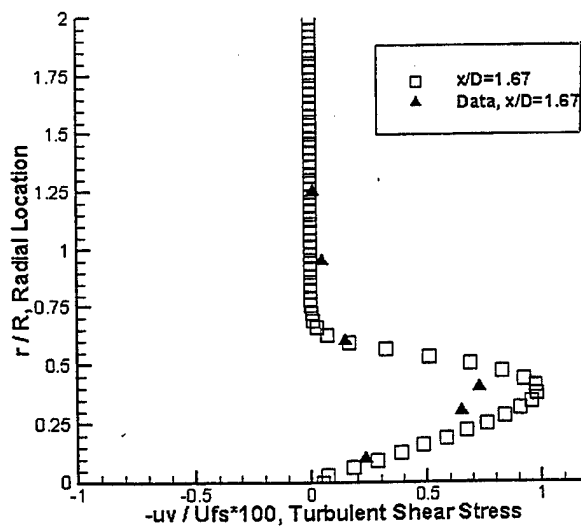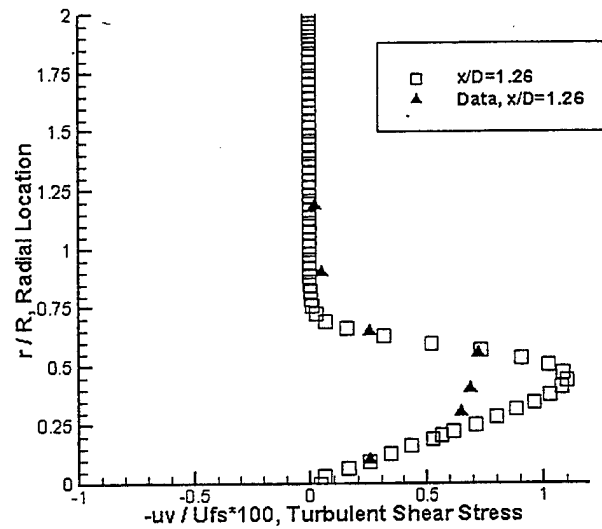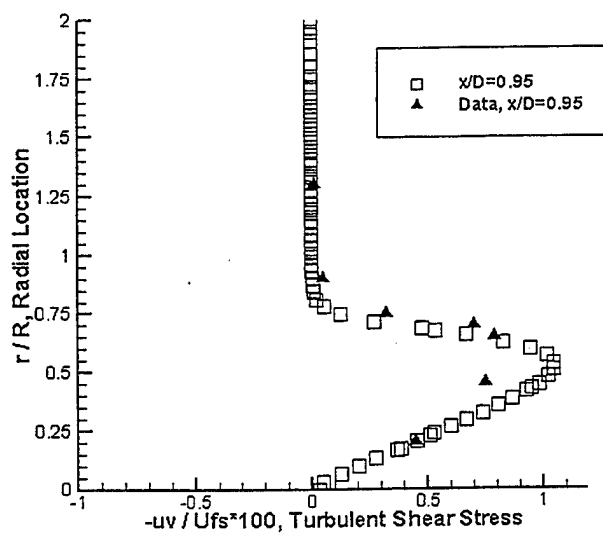
Figure 13. Turbulent shear stress (−uv/Ufs^2) as a function of radial position (r/R) for various downstream locations (compared to experimental data) for base bleed (I = 0.01).
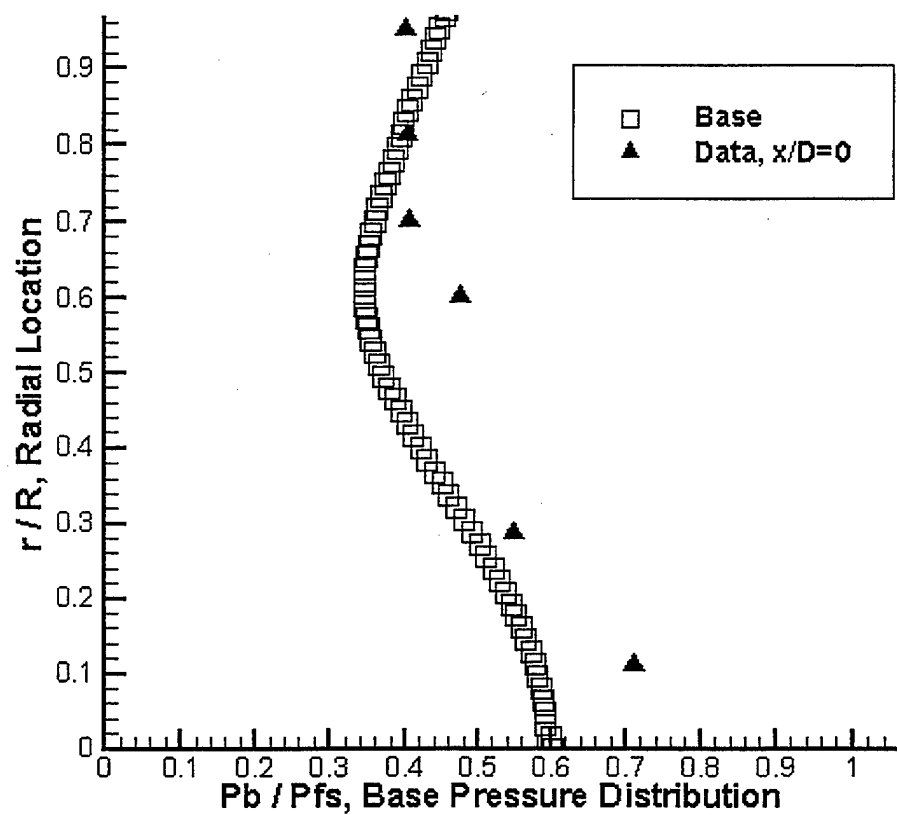
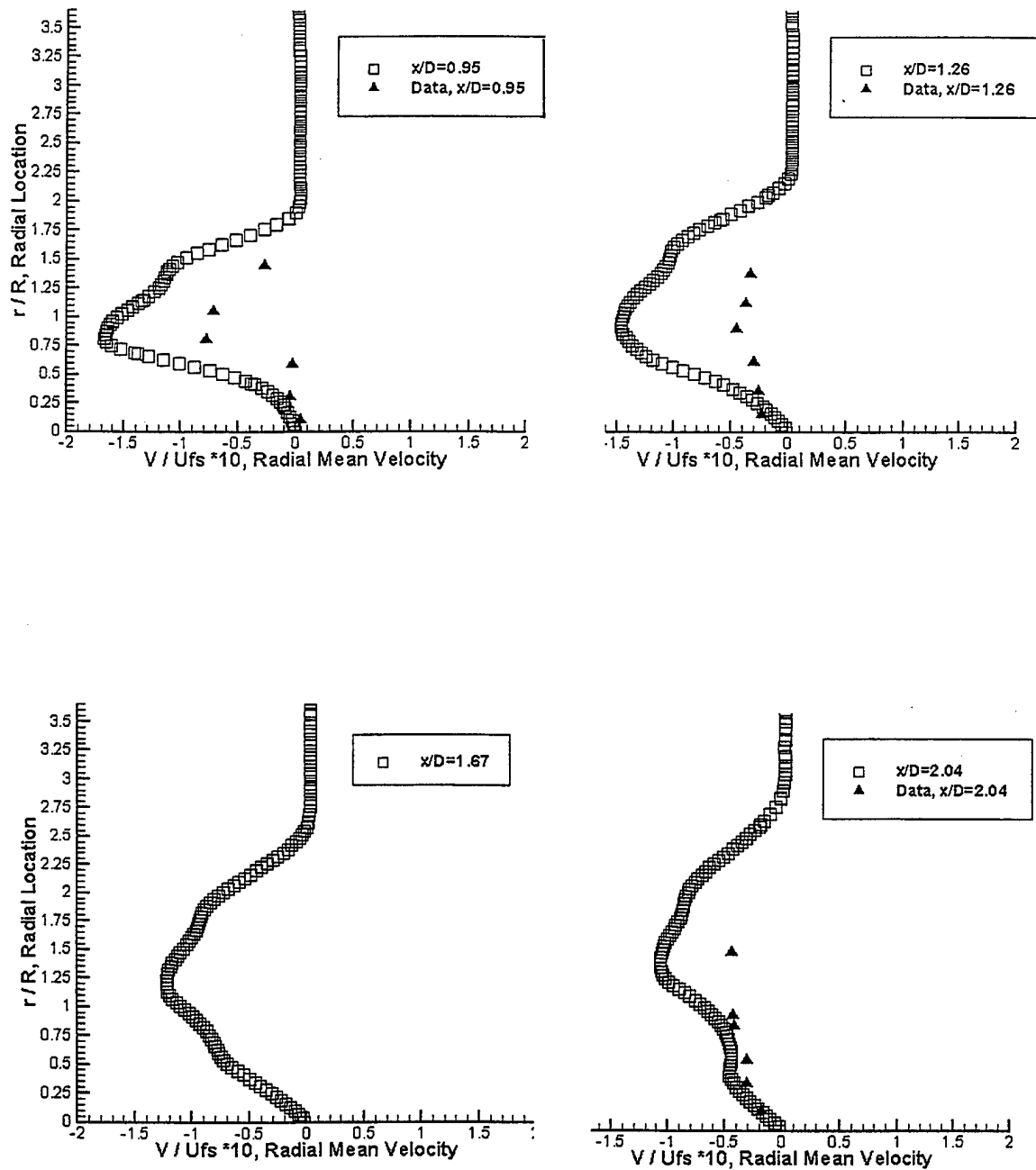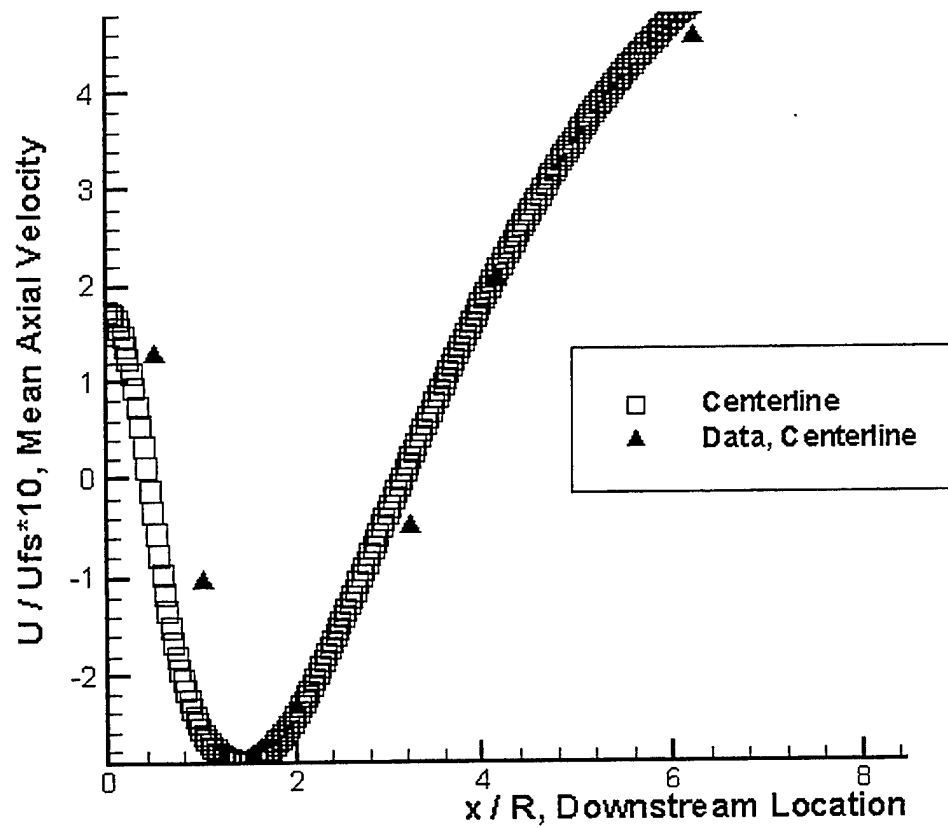Figure 14. Streamwise mean velocity, U/Ufs, vs. downstream location x/R, for base
bleed (I = 0.01) with comparison to experimental data.
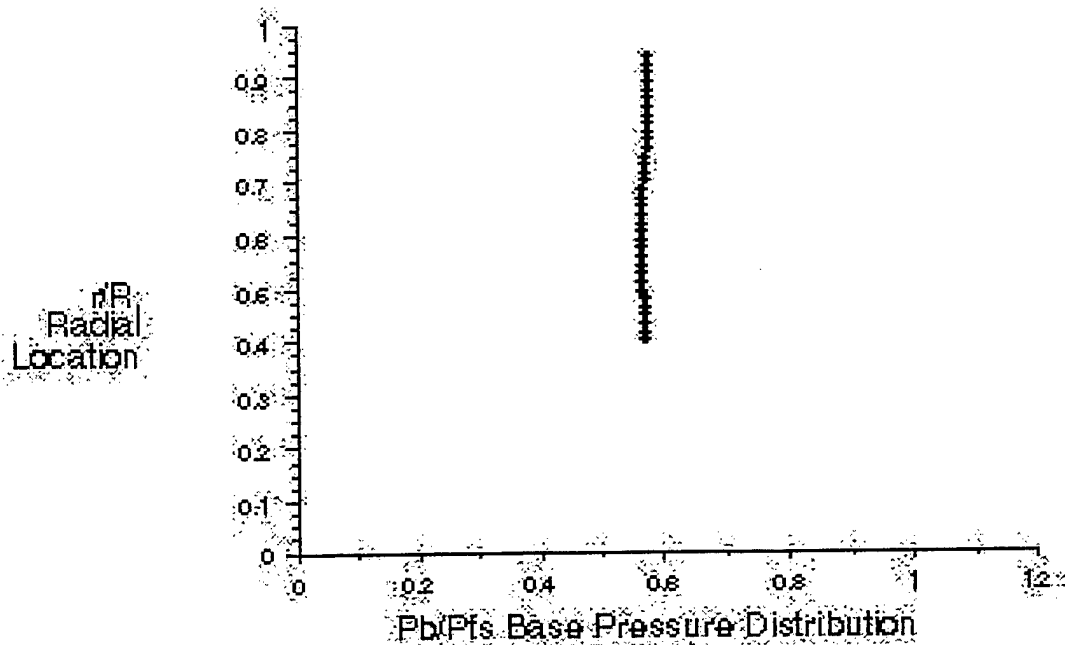
Figure 15. Base pressure profile for base bleed (I = 0.01).
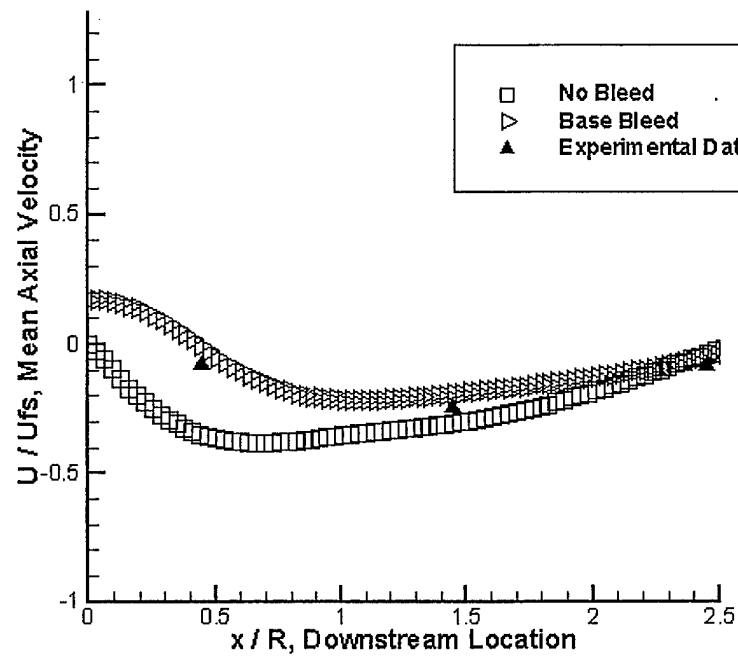
Figure 16. Streamwise mean velocity, U/Ufs, as a function of downstream location, x/R, for no base bleed and base bleed (I = 0.01) with comparison to experimental data.
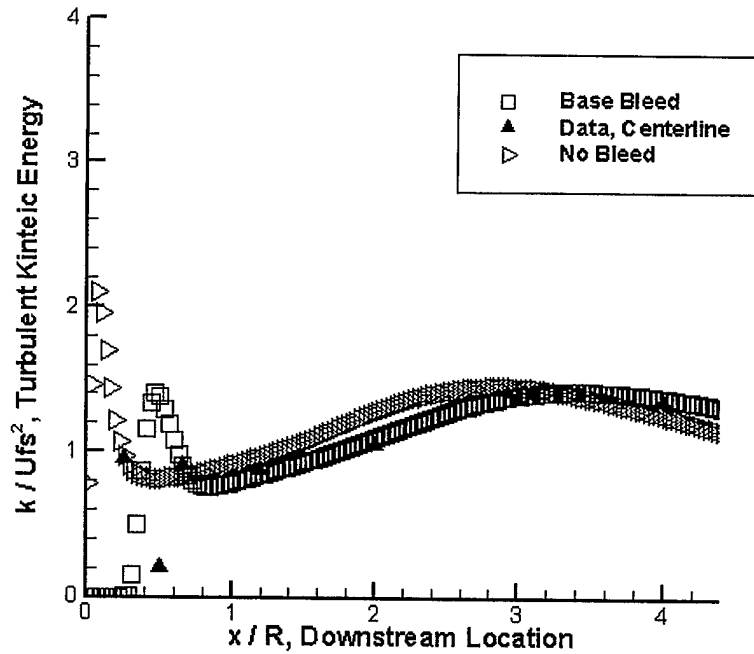
Figure 17. Turbulent kinetic energy, k/Ufs^2, vs. downstream location, x/R, for no bleed and base bleed (I = 0.01) with comparison to experimental data.
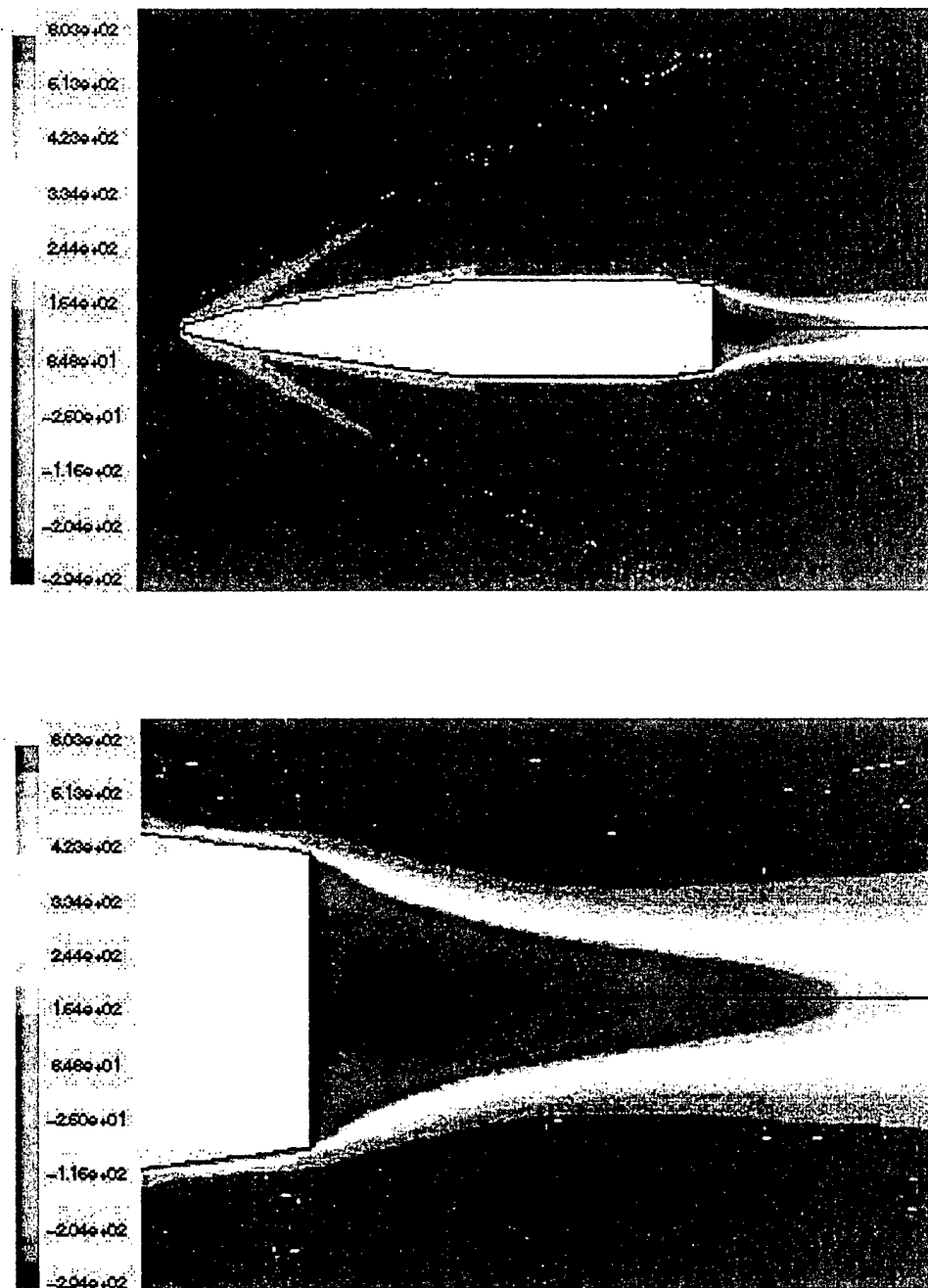
Figure 18. Contours of mean axial velocity for M549 projectile.
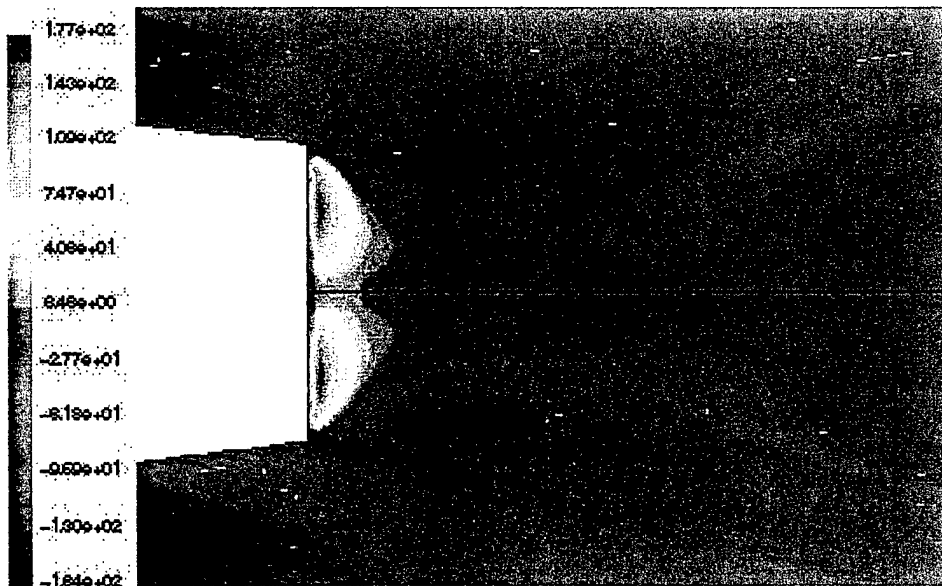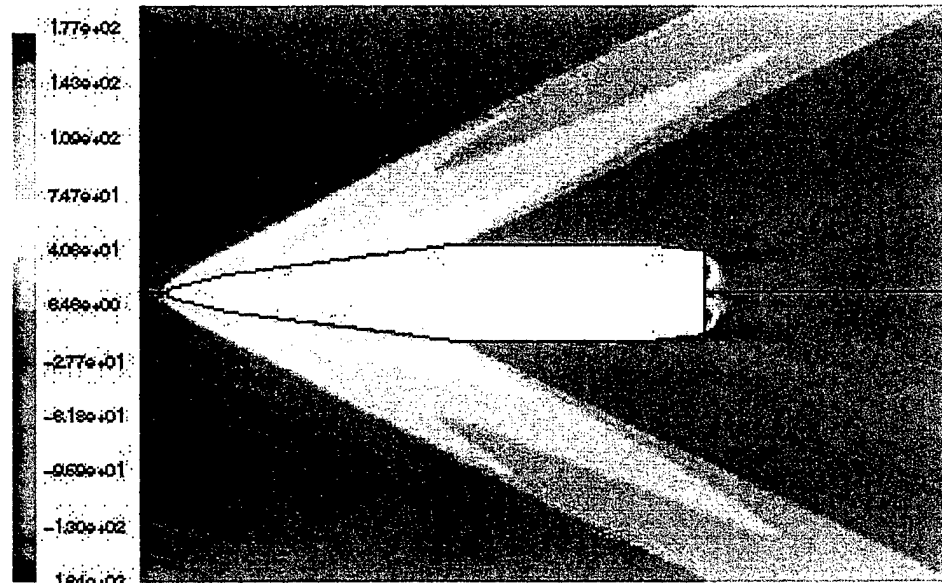
Figure 19. Contours of mean radial velocity for M549 projectile.
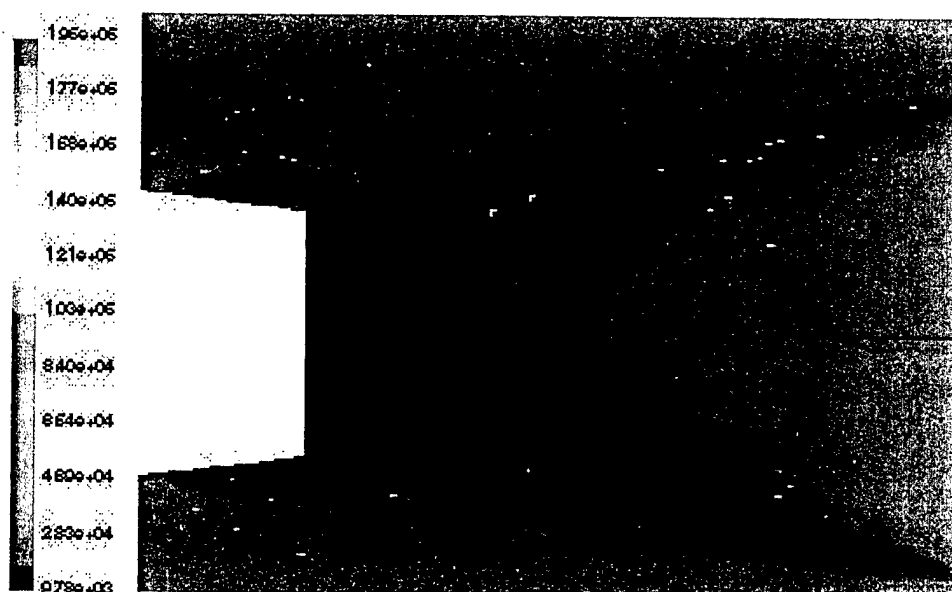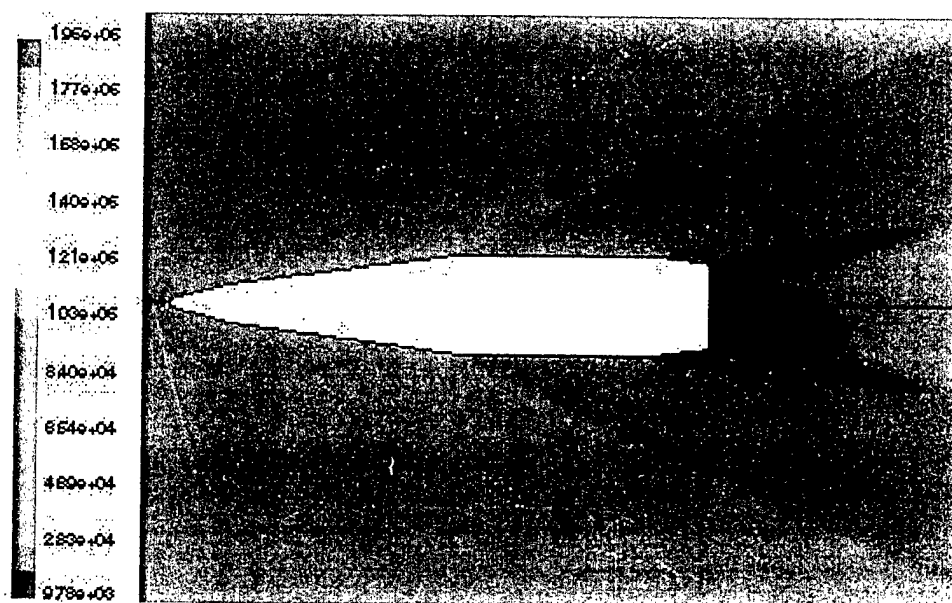
Figure 20. Contours of static pressure for M549 projectile.

26
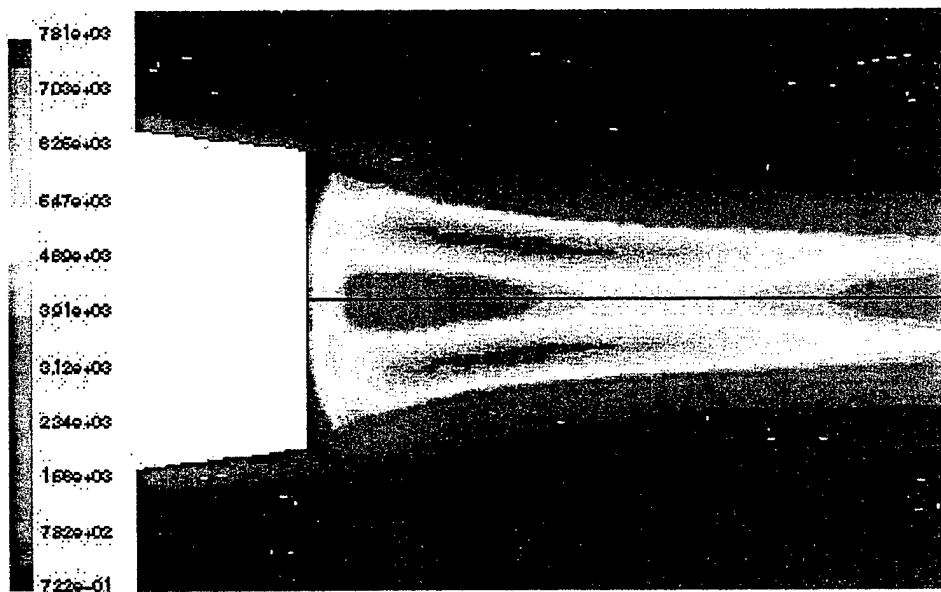
Figure 21. Contours of turbulent kinetic energy for M549 projectile.
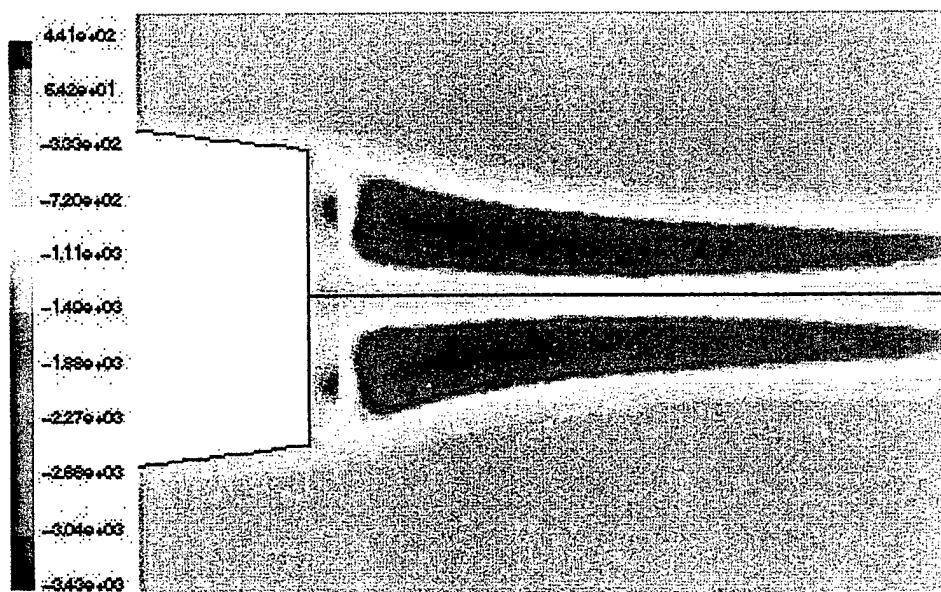
Figure 22. Contours of turbulent shear stress for M549 projectile.
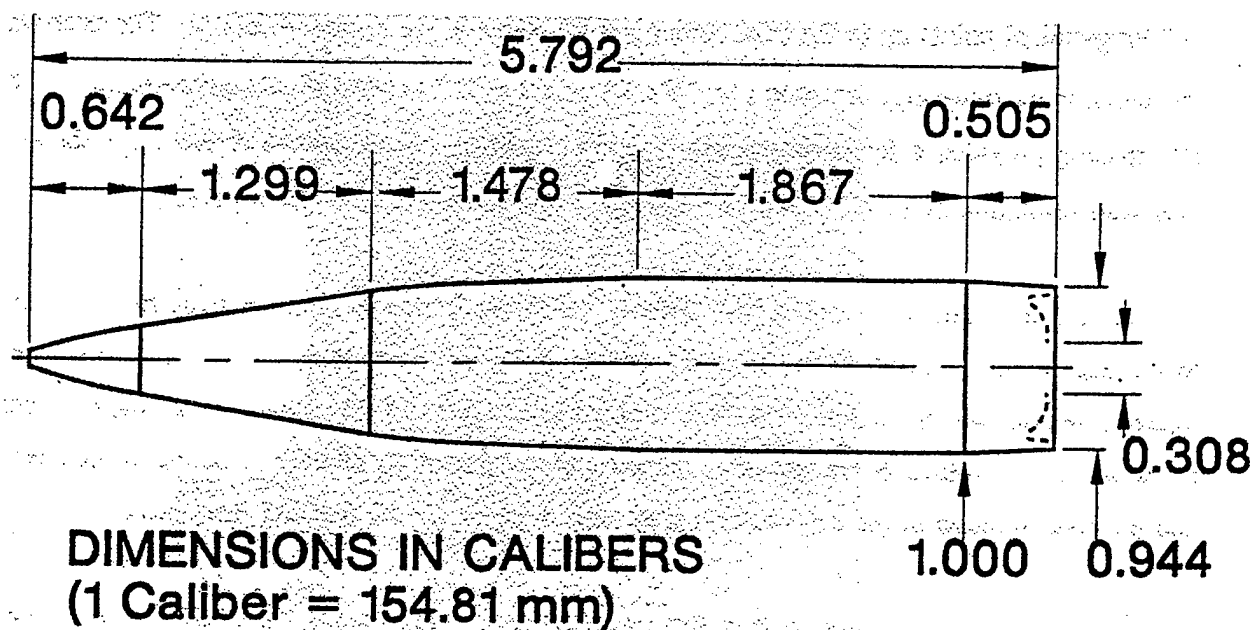
Figure 23. Schematic of M864 projectile.

28

No Combustion

2.88e+02
2.56e+02
2.25e+02
1.93e+02
1.62e+02
1.30e+02
9.91e+01
6.76e+01
3.62e+01
4.78e+00
-2.66e+01

Combustion

3.84e+02
3.38e+02
2.92e+02
2.46e+02
2.00e+02
1.54e+02
1.08e+02
6.18e+01
1.58e+01
-3.02e+01
-7.62e+01
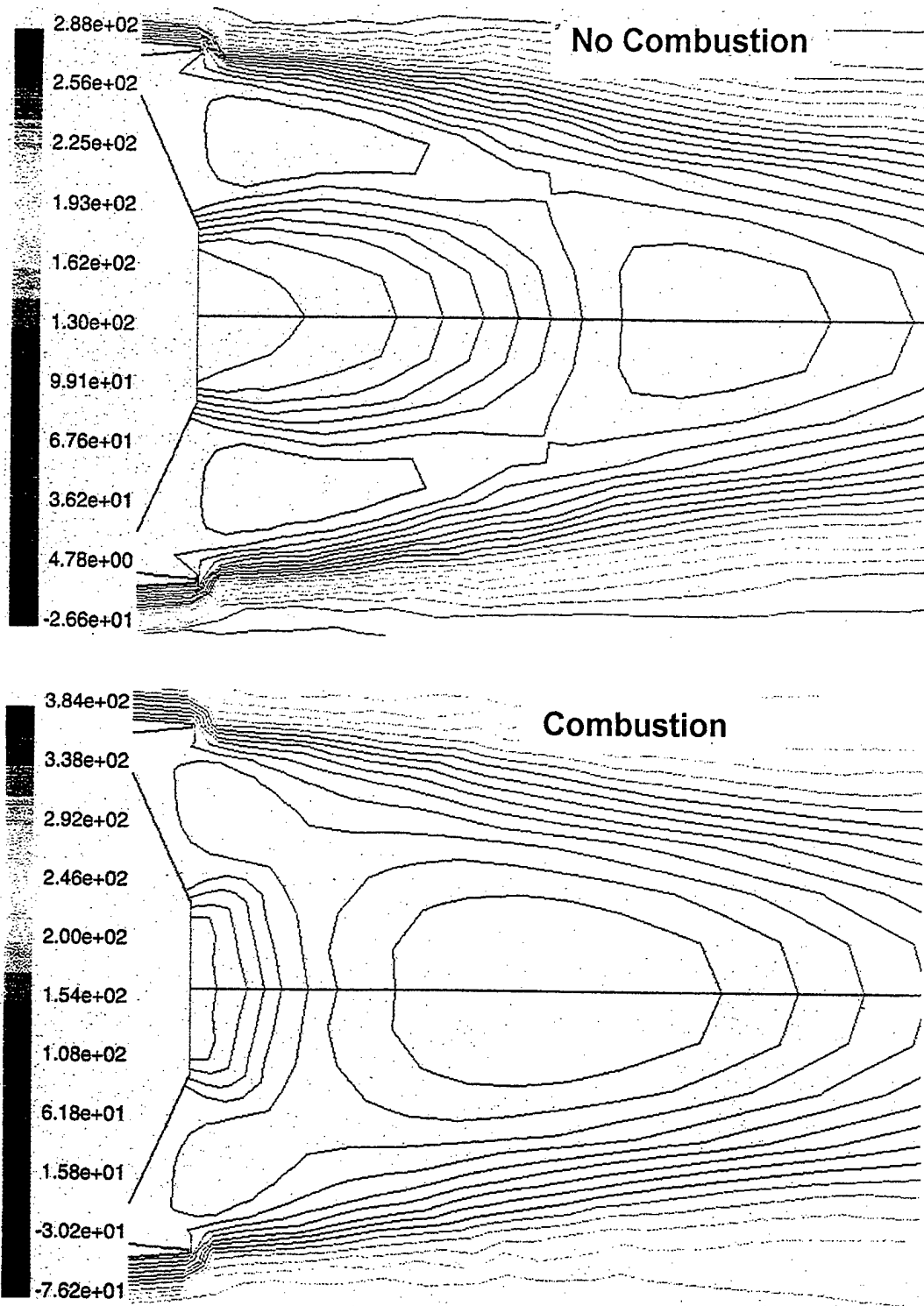
Figure 24. Contours of mean axial velocity for M = 0.8 without and with wake combustion.
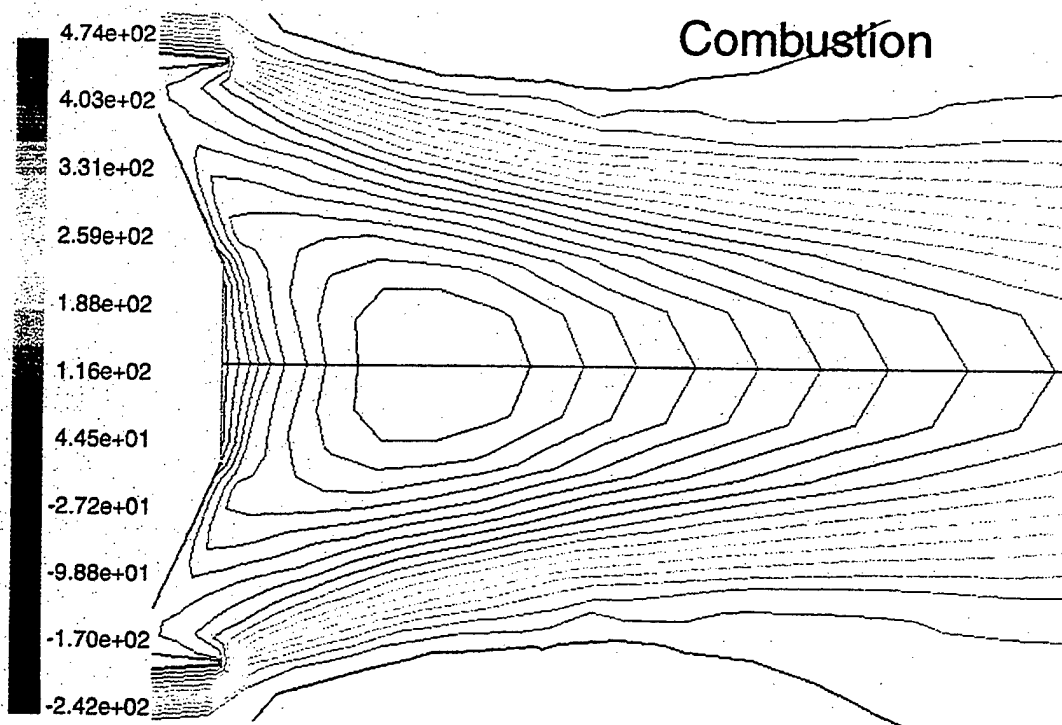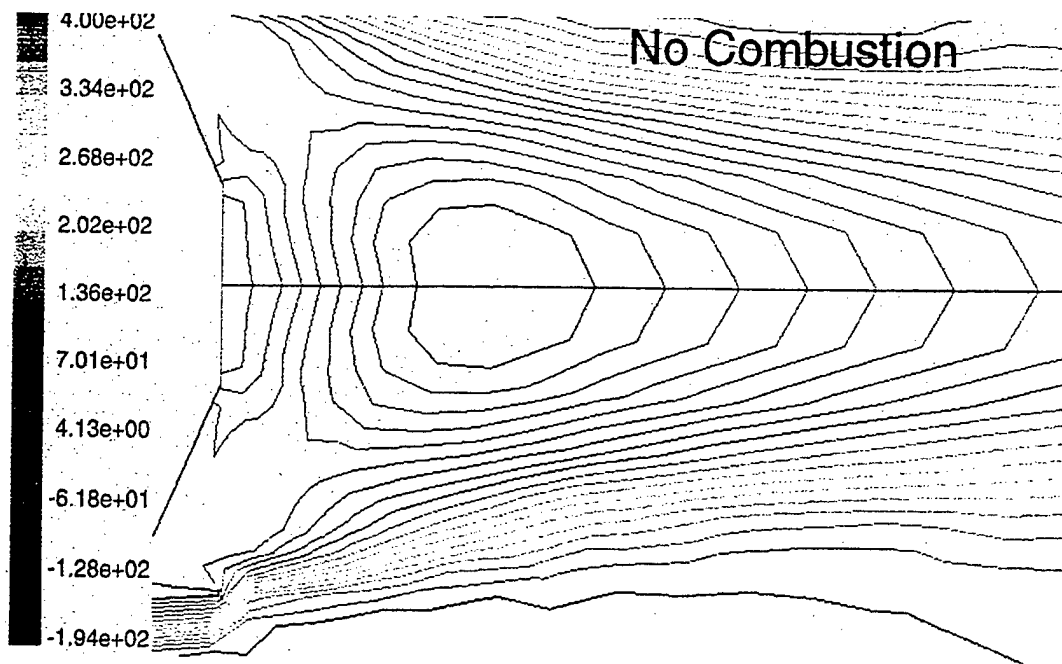
Figure 25. Contours of mean axial velocity for M = 1.5 without and with wake combustion.

No Combustion

5.44e+02
4.47e+02
3.49e+02
2.51e+02
1.53e+02
5.55e+01
-4.22e+01
-1.40e+02
-2.38e+02
-3.35e+02

Combustion

6.42e+02
5.41e+02
4.41e+02
3.40e+02
2.39e+02
1.38e+02
3.72e+01
-6.36e+01
-1.64e+02
-2.65e+02
-3.66e+02
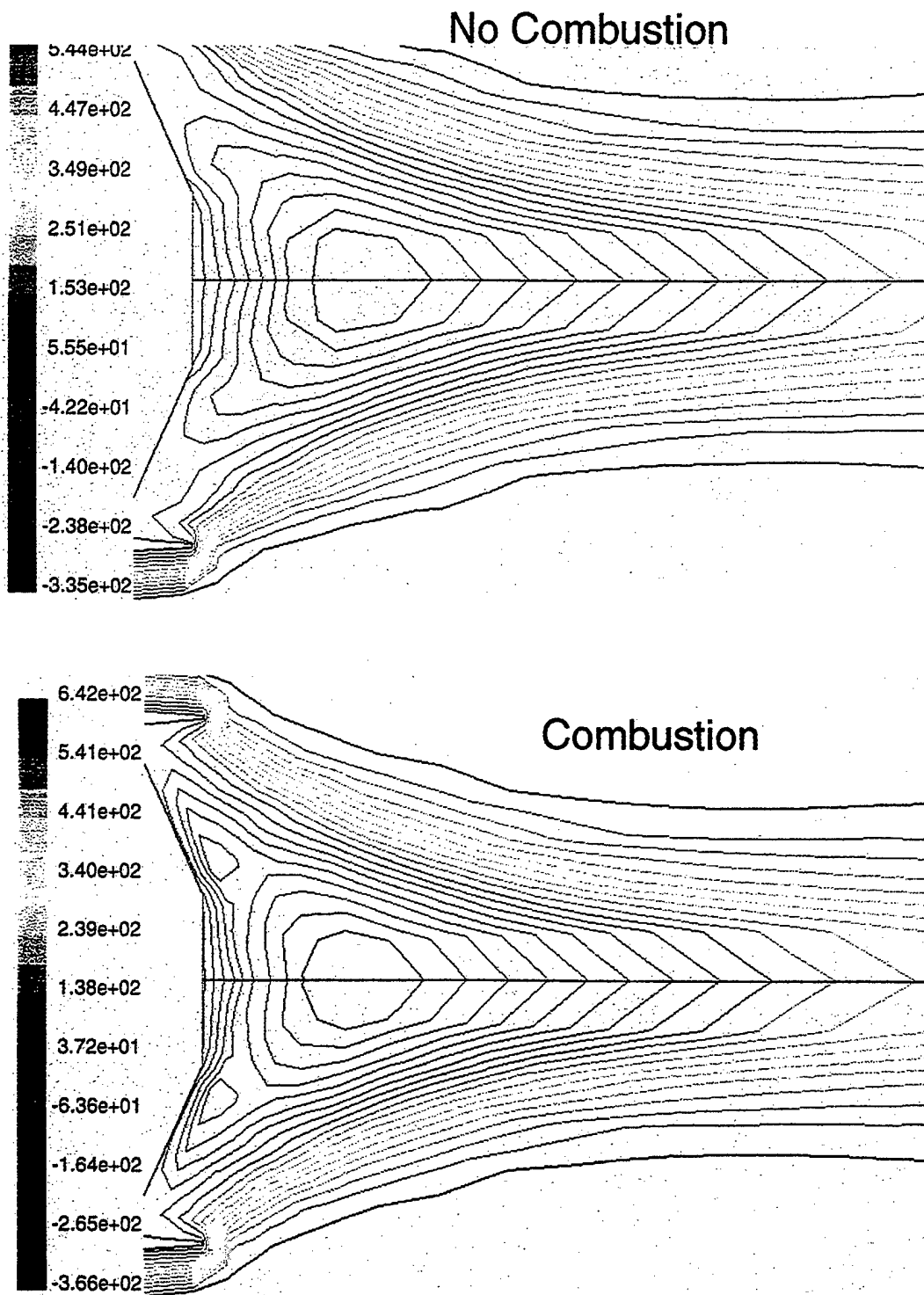
Figure 26. Contours of mean axial velocity for M = 3.0 without and with wake combustion.

No Combustion

9.29e+01

7.35e+01

5.42e+01

3.49e+01

1.56e+01

-3.71e+00

-2.30e+01

-4.23e+01

-6.16e+01 ▽

-8.10e+01

Combustion

1.61e+02

1.31e+02

1.01e+02

7.06e+01

4.06e+01

1.06e+01

-1.95e+01

-4.95e+01

-7.95e+01

-1.10e+02
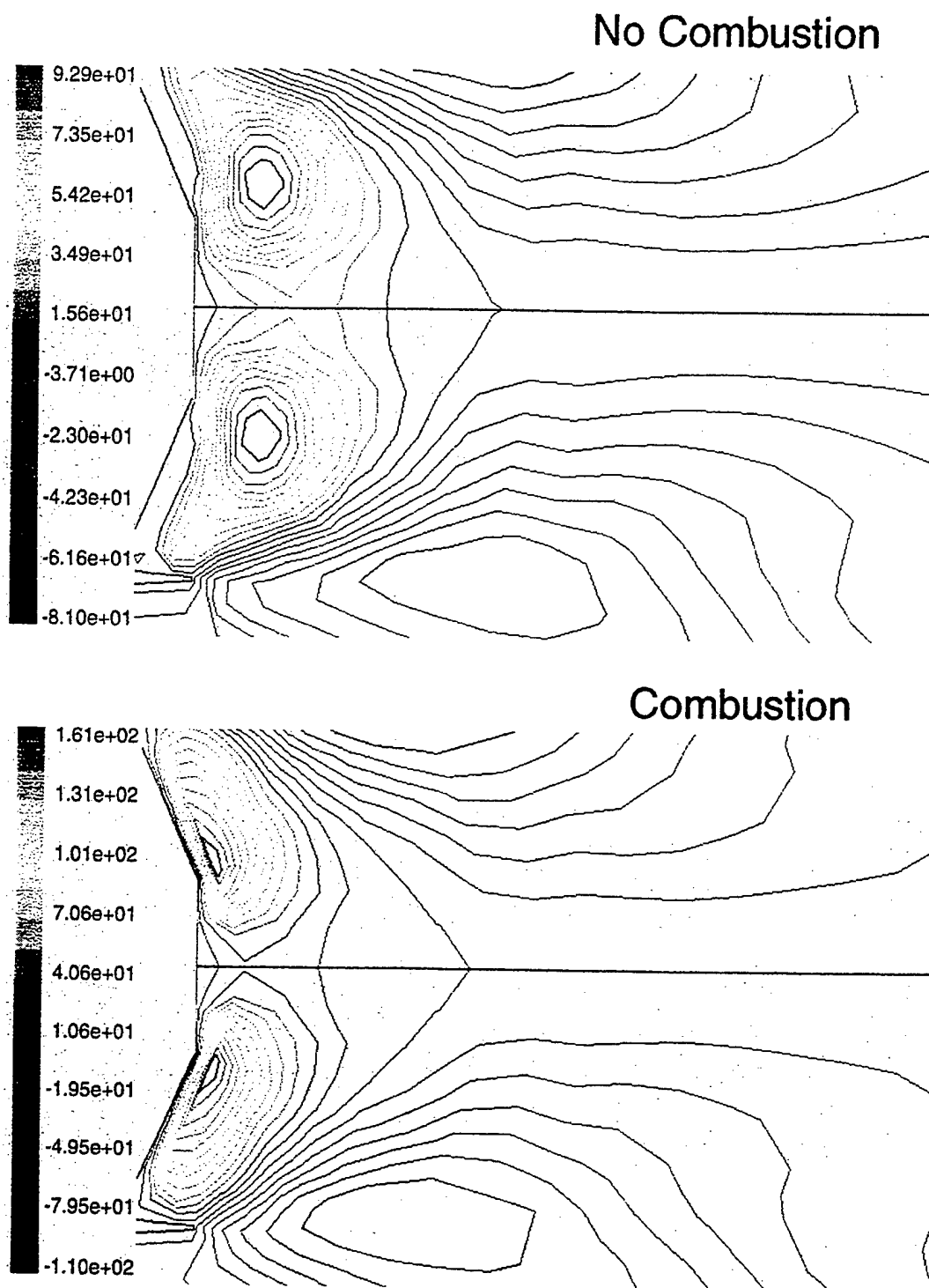
Figure 27. Contours of mean radial velocity for M = 1.5 without and with wake combustion.

No Combustion

■	1.95e+02
▨	1.51e+02
░	1.07e+02
▒	6.30e+01
▓	1.90e+01
■	-2.51e+01
■	-6.92e+01
■	-1.13e+02
■	-1.57e+02
■	-2.01e+02

Combustion

■	3.19e+02
▨	2.56e+02
░	1.94e+02
▒	1.32e+02
▓	6.96e+01
■	7.35e+00
■	-5.49e+01
■	-1.17e+02
■	-1.79e+02
■	-2.42e+02
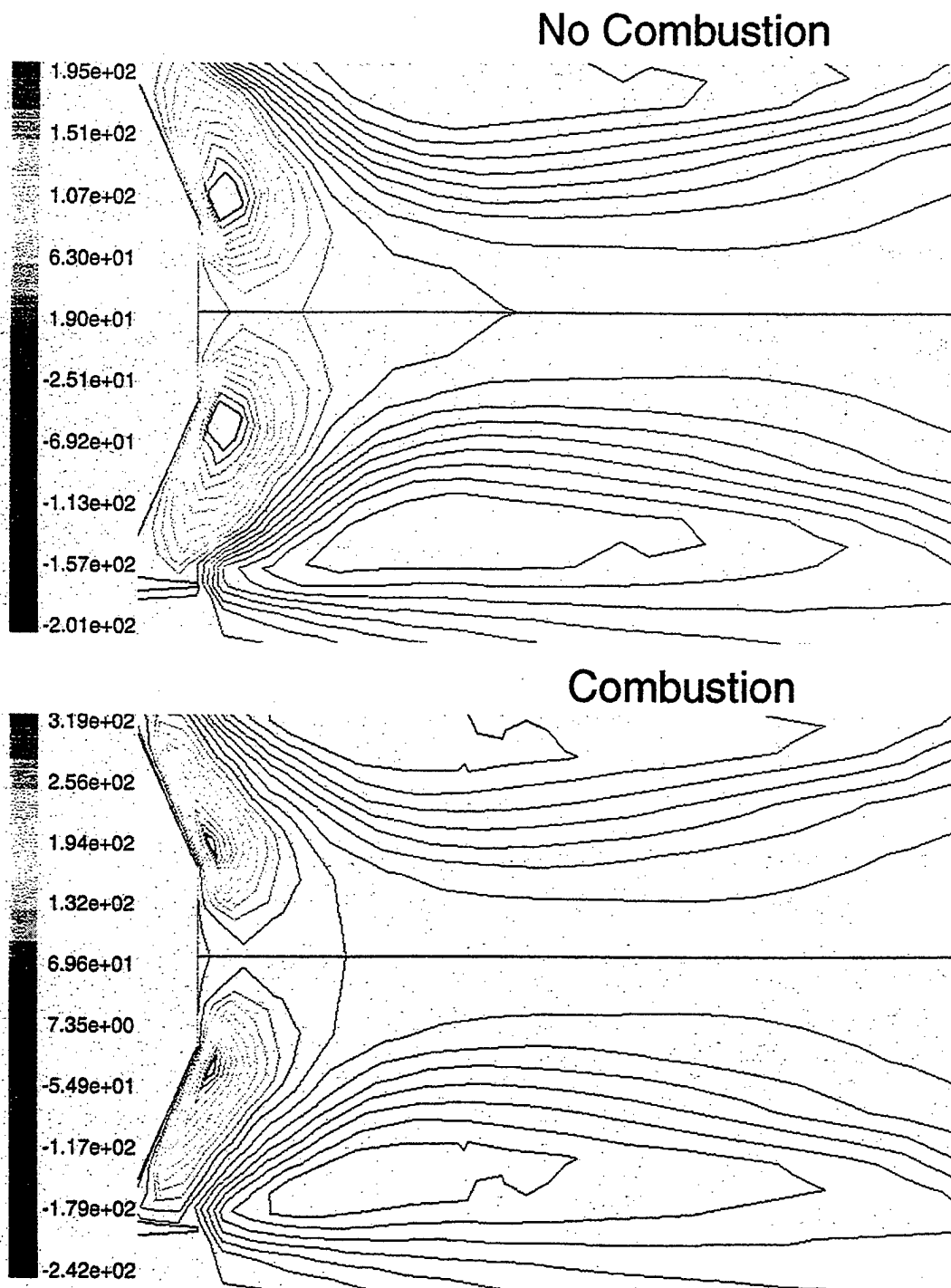
Figure 28. Contours of mean radial velocity for M = 3.0 without and with wake combustion.

No Combustion

1.83e+03
1.63e+03
1.42e+03
1.22e+03
1.02e+03
8.14e+02
6.11e+02
4.07e+02
2.04e+02
6.82e-01

Combustion

2.14e+03
1.91e+03
1.67e+03
1.43e+03
1.19e+03
9.53e+02
7.15e+02
4.77e+02
2.39e+02
6.62e-01
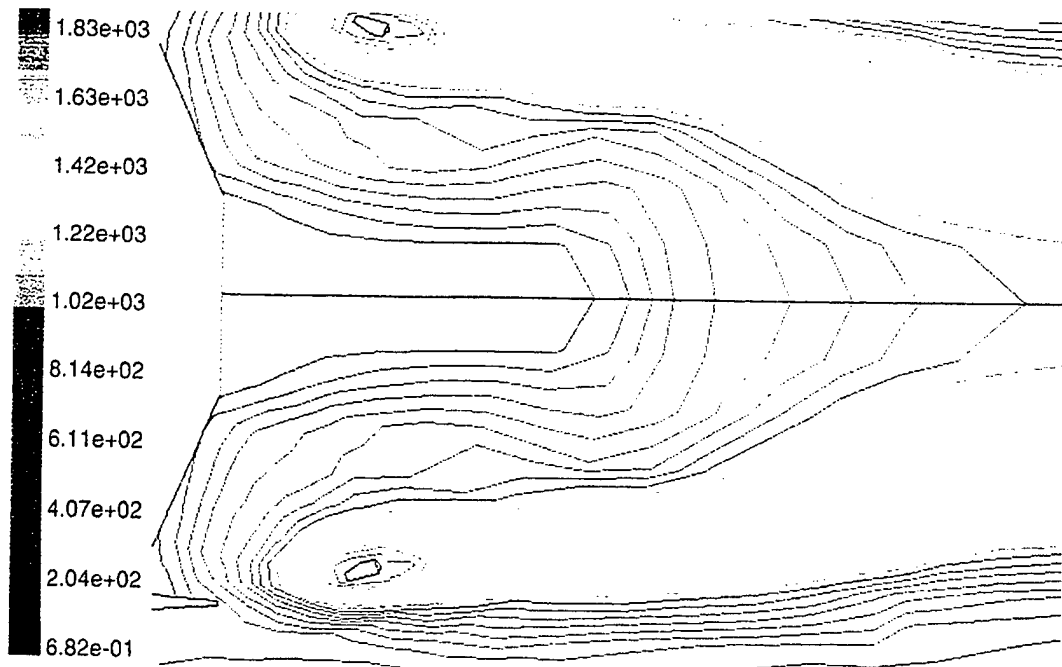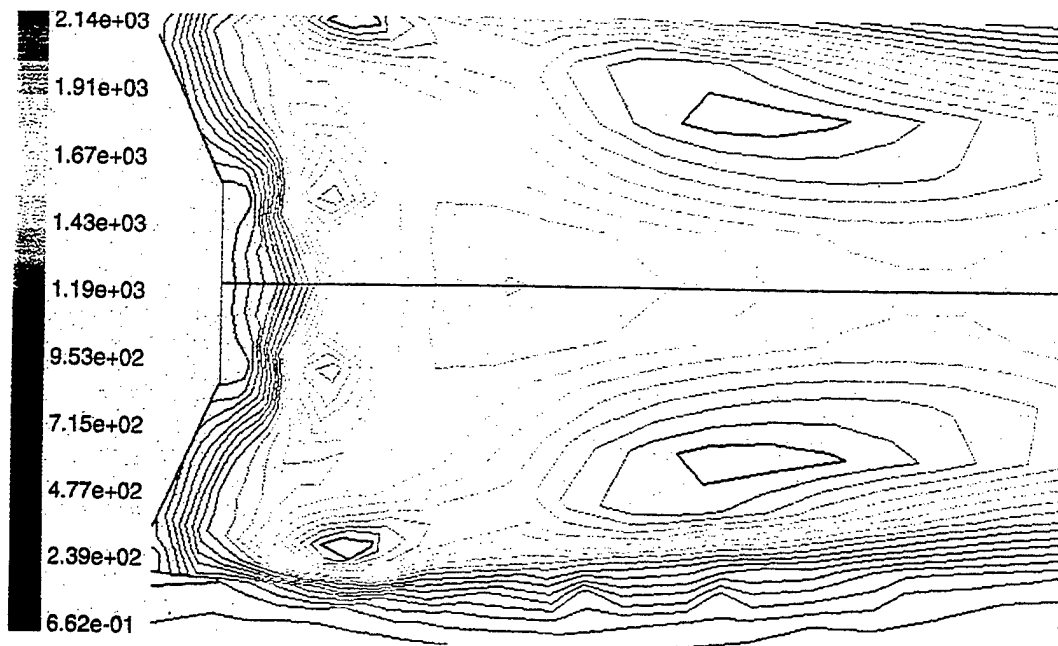
Figure 29. Contours of turbulent kinetic energy for M = 0.8 without and with wake combustion.

34

No Combustion

4.42e+03
3.79e+03
3.15e+03
2.52e+03
1.89e+03
1.26e+03
6.31e+02
7.50e-01

Combustion

6.85e+03
6.17e+03
5.48e+03
4.80e+03
4.11e+03
3.43e+03
2.74e+03
2.06e+03
1.37e+03
6.86e+02
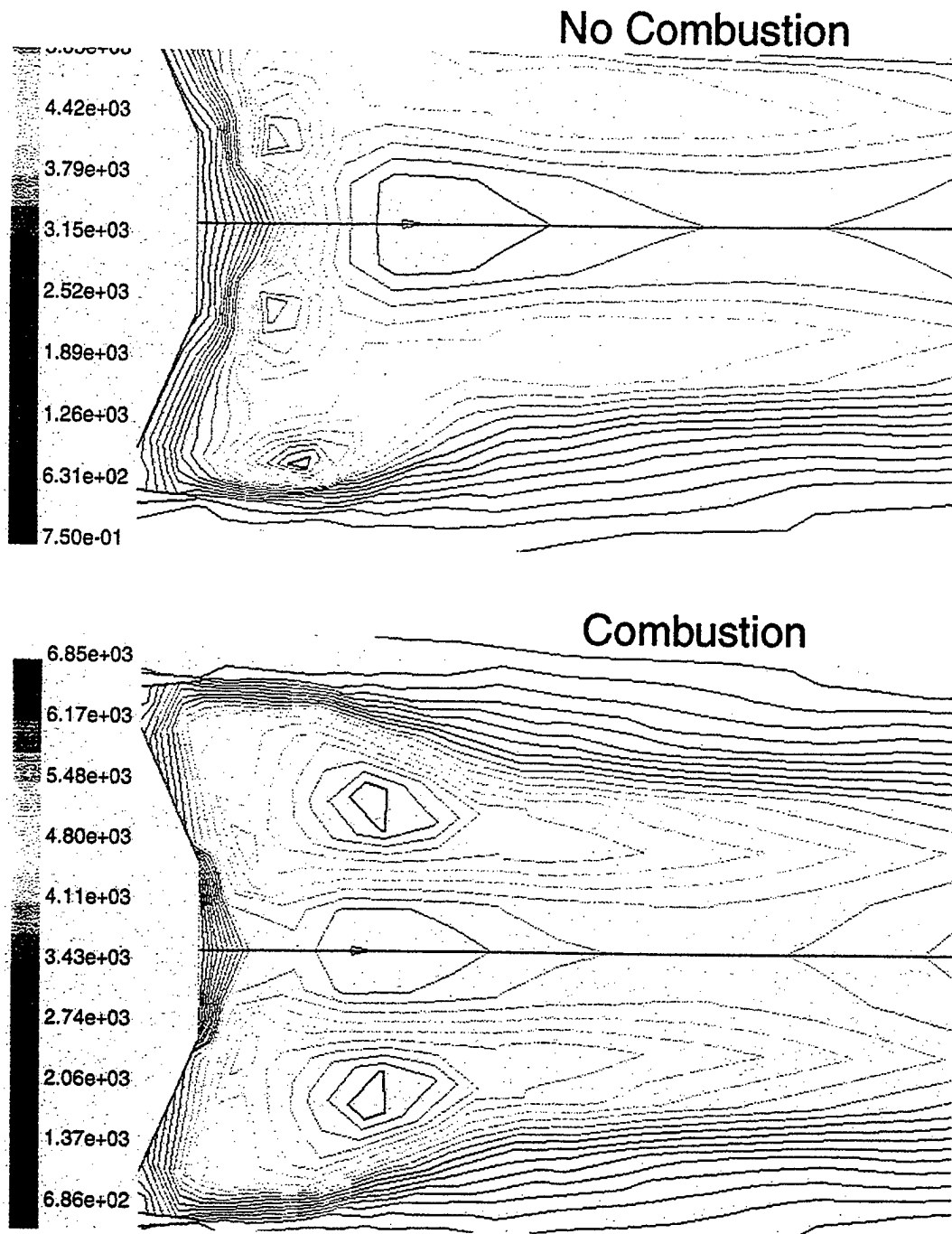
Figure 30. Contours of turbulent kinetic energy for M = 1.5 without and with wake combustion.

35
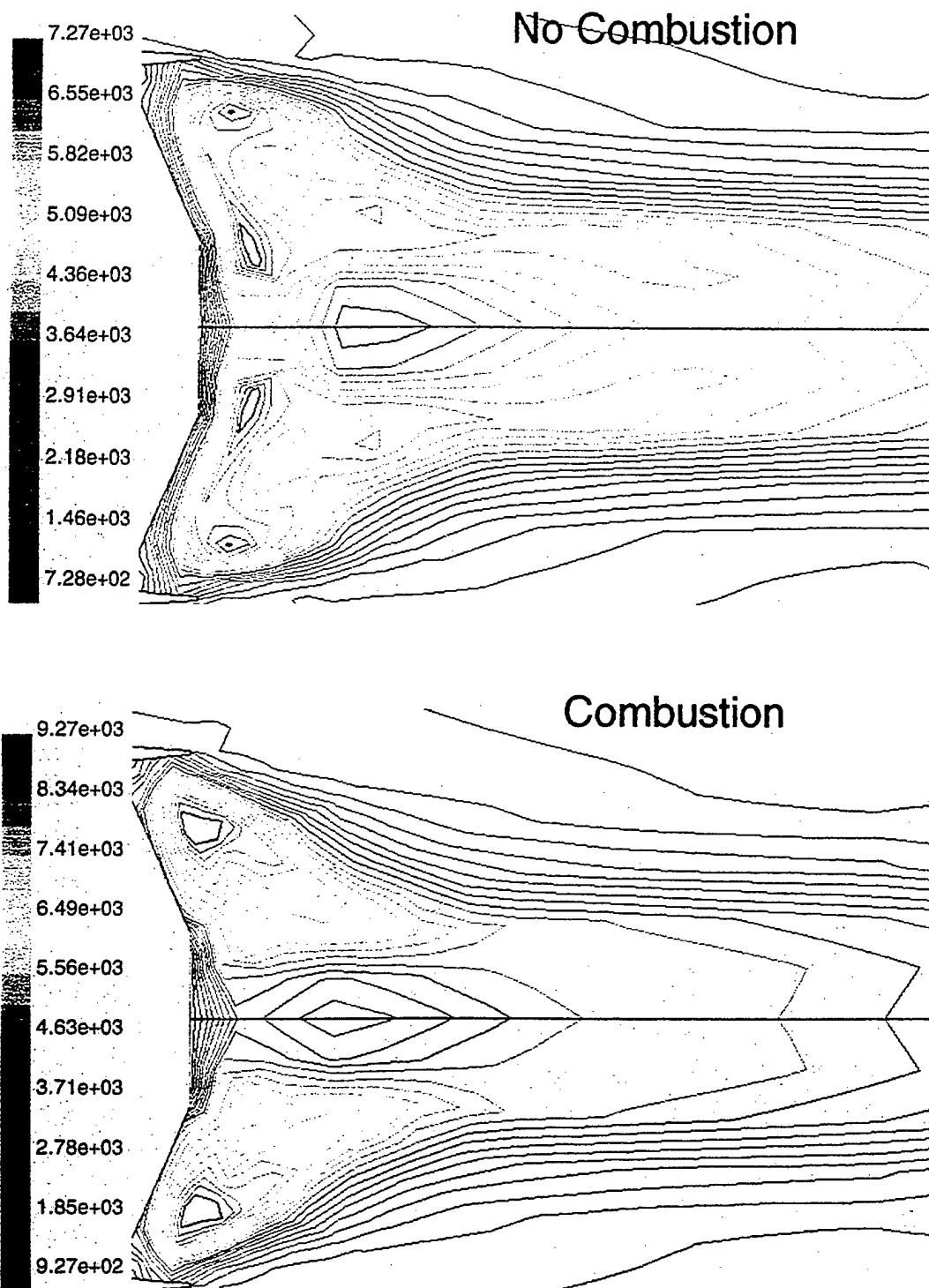
Figure 31. Contours of turbulent kinetic energy for M = 3.0 without and with wake combustion.

No Combustion

1.85e+02

7.81e+01

-2.85e+01

-1.35e+02

-2.42e+02

-3.48e+02

-4.55e+02

-5.61e+02

-6.68e+02

-7.75e+02

Combustion

3.37e+02

1.98e+02

5.90e+01

-7.97e+01

-2.18e+02

-3.57e+02

-4.96e+02

-6.35e+02

-7.73e+02

-9.12e+02
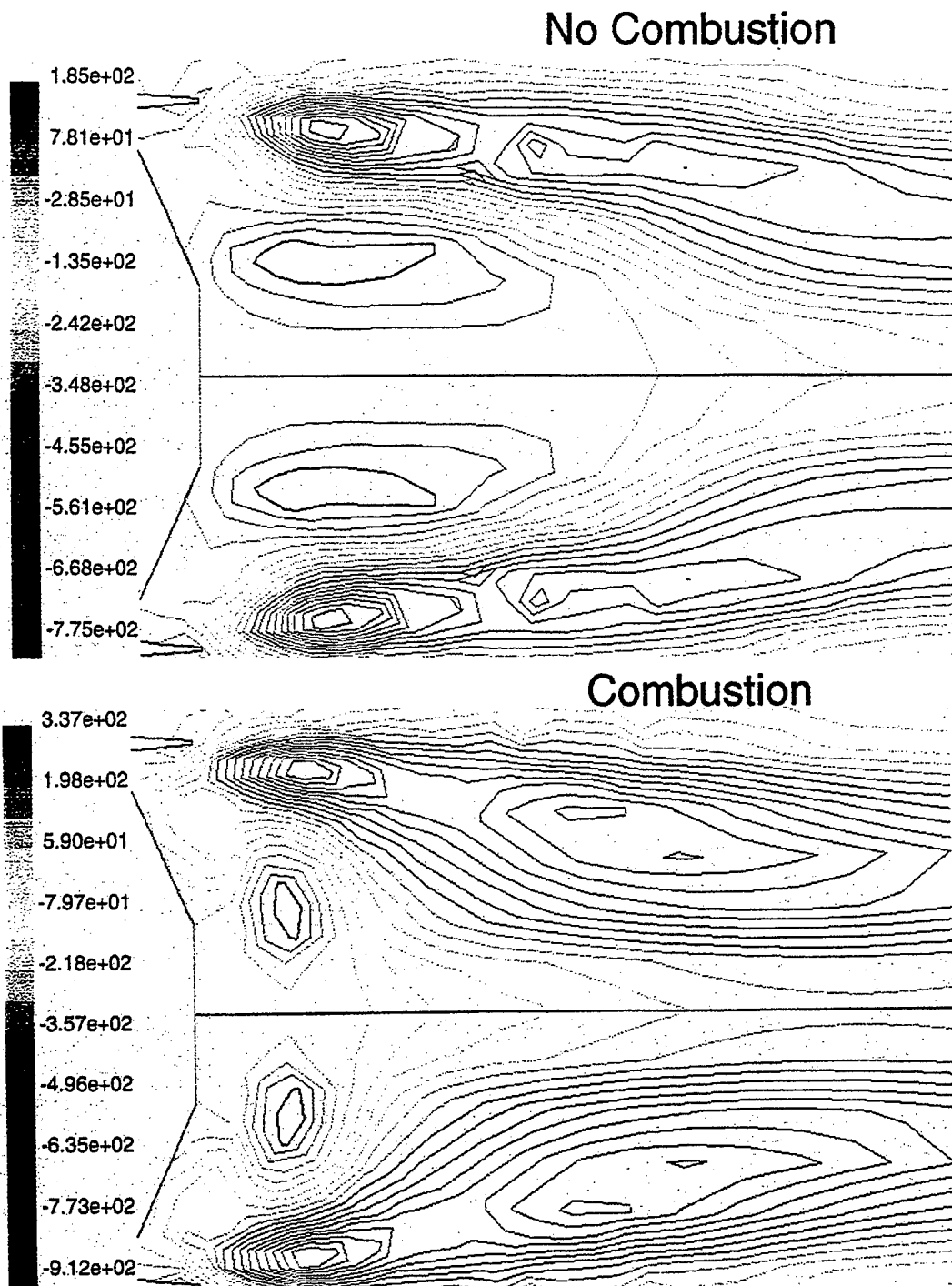
Figure 32. Contours of turbulent shear stress for M = 0.8 without and with wake combustion.

37
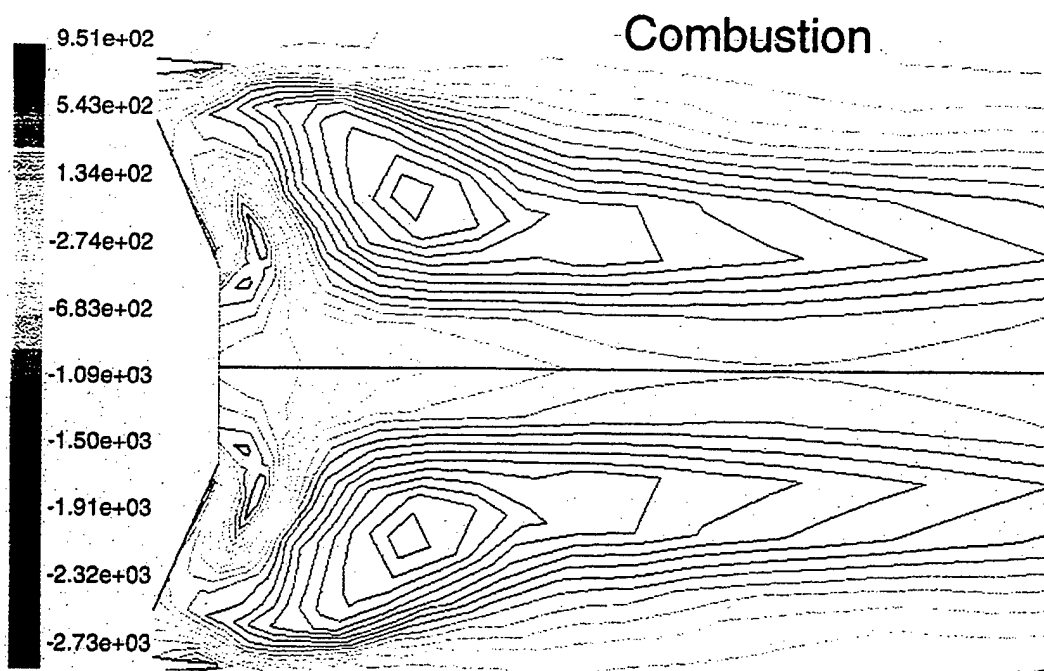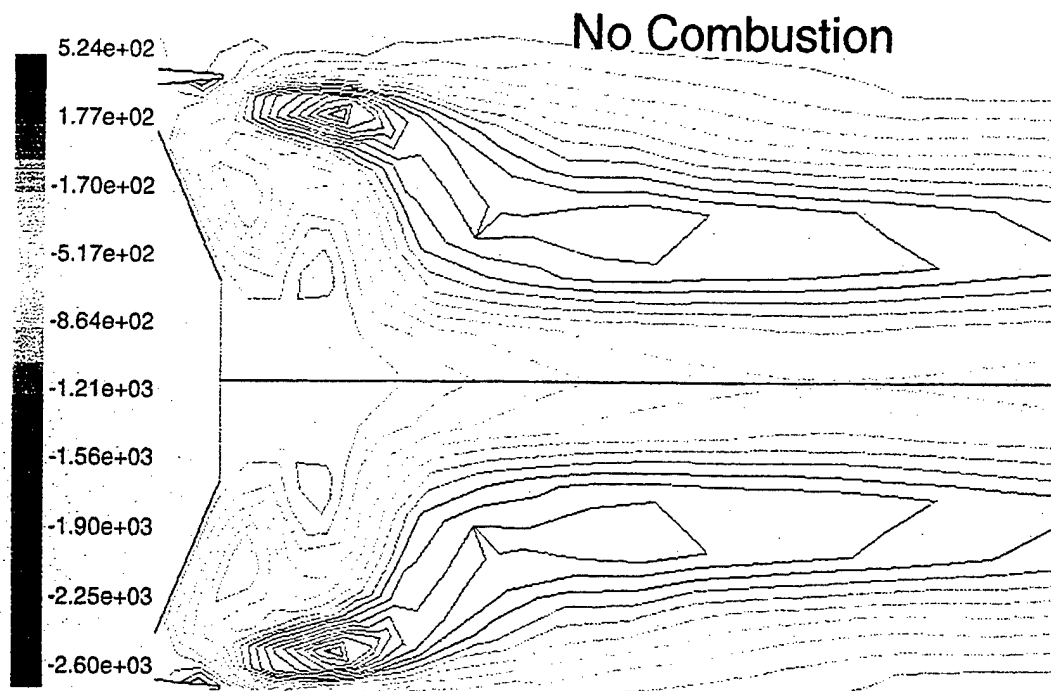
Figure 33. Contours of turbulent shear stress for M = 1.5 without and with wake combustion.

No Combustion

1.17e+03
7.86e+02
4.03e+02
2.03e+01
-3.62e+02
-7.45e+02
-1.13e+03
-1.51e+03
-1.89e+03
-2.28e+03

Combustion

1.36e+03
8.93e+02
4.22e+02
-4.87e+01
-5.20e+02
-9.91e+02
-1.46e+03
-1.93e+03
-2.40e+03
-2.87e+03
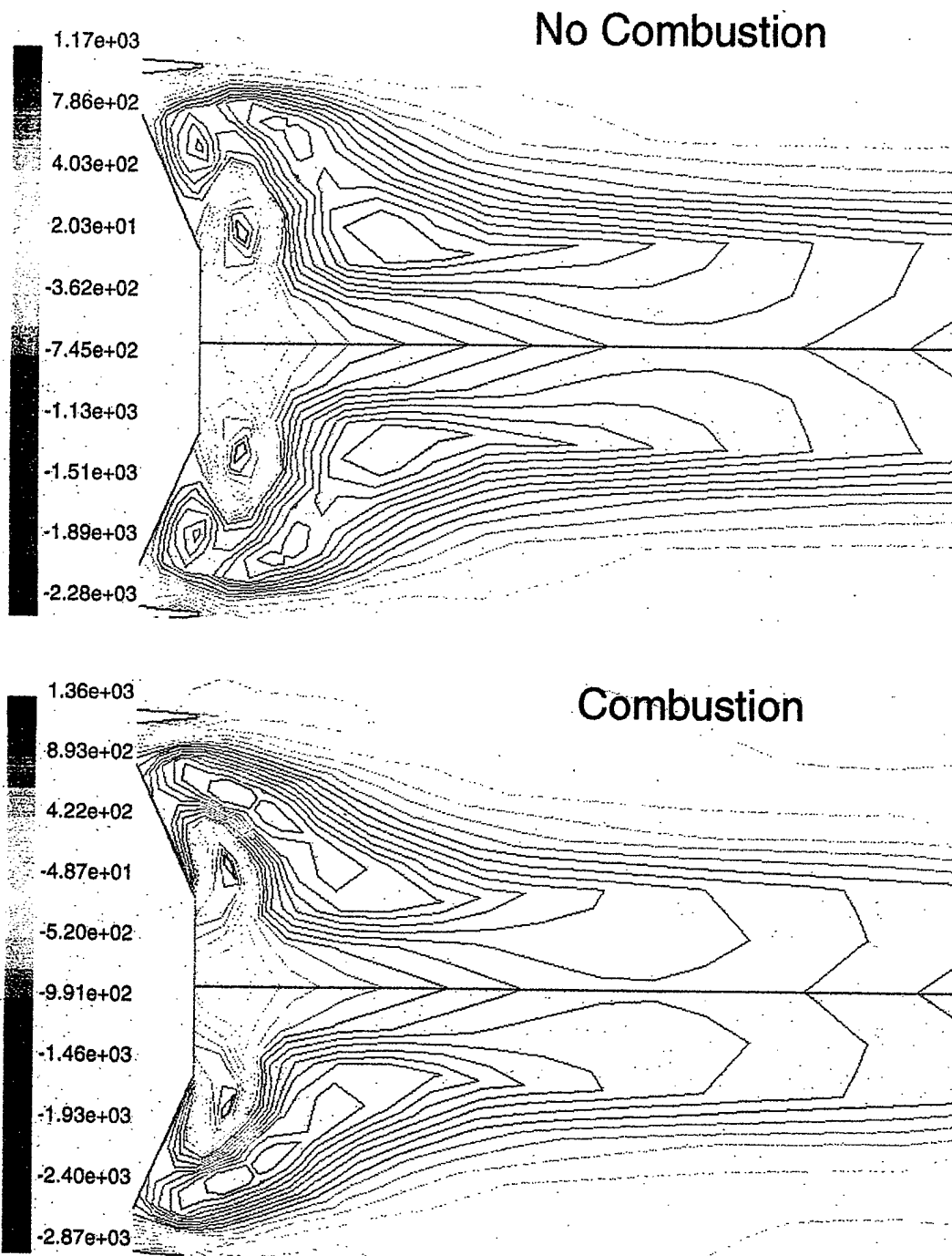
Figure 34. Contours of turbulent shear stress for M = 3.0 without and with wake combustion.

39

3.58e+00
3.22e+00
2.87e+00
2.52e+00
2.17e+00
1.82e+00
1.46e+00
1.11e+00
7.60e-01
4.08e-01
5.56e-02
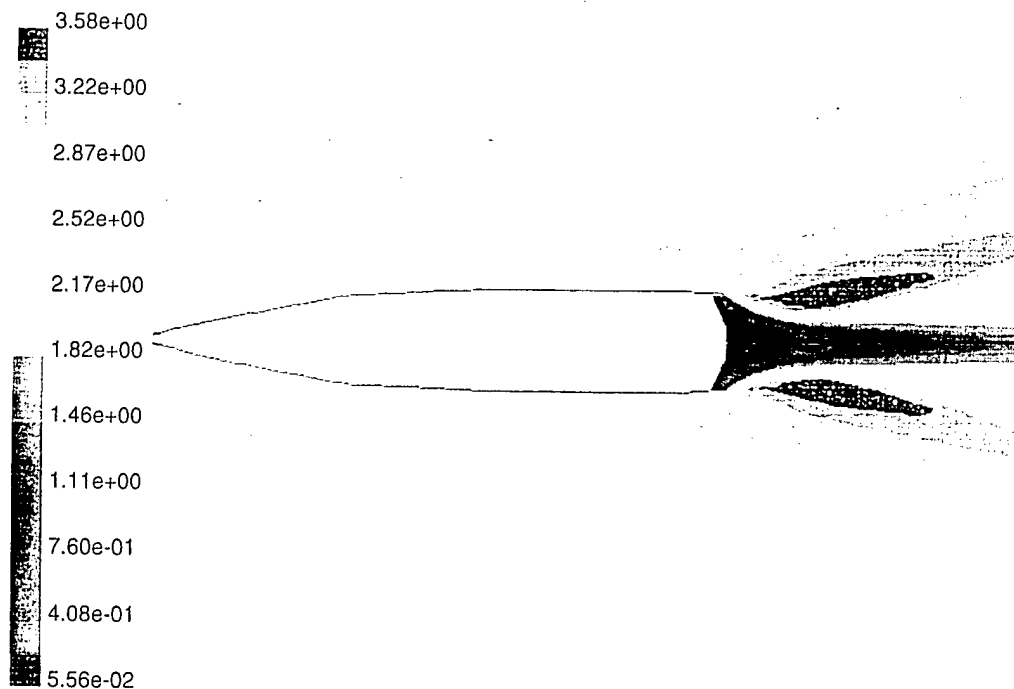
Mar 31, 2000
FLUENT 5.3 (axi, coupled imp, RSM)

Figure 35. Contours of Mach number for M = 3.0 with wake combustion.

6.05e+02
5.19e+02
4.32e+02
3.45e+02
2.59e+02
1.72e+02
8.57e+01
-9.53e-01
-8.76e+01
-1.74e+02
-2.61e+02
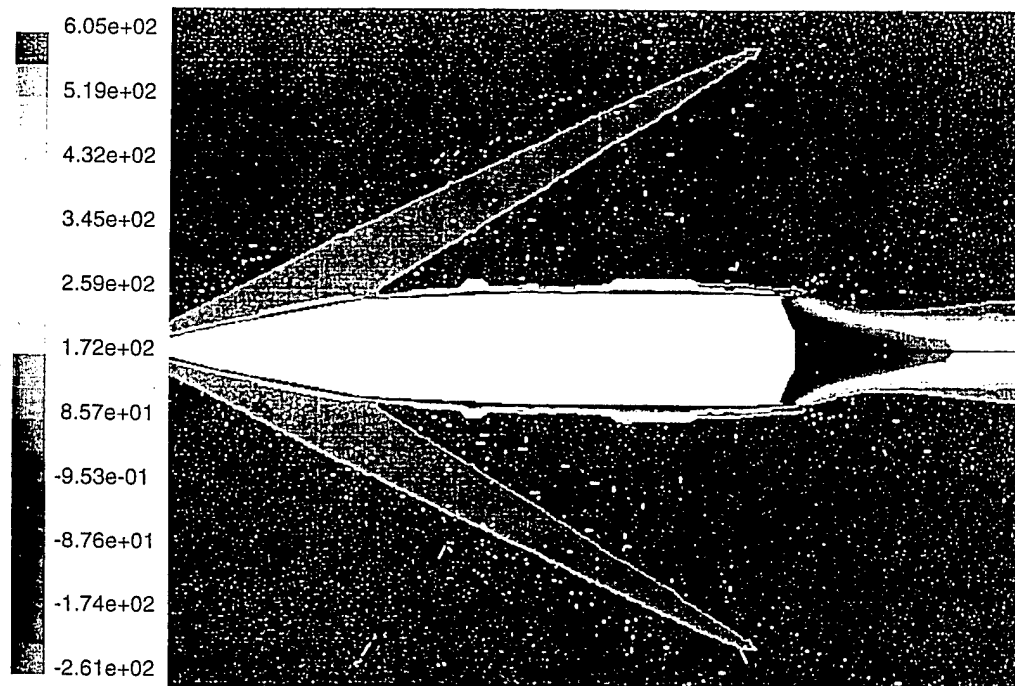
Mar 28, 2000
FLUENT 5.3 (axi, coupled imp, S-A)

Figure 36. Contours of axial mean velocity for M = 3.0 with wake combustion.

40

6.42e+02	
5.44e+02	
4.47e+02	
3.49e+02	
2.51e+02	
1.53e+02	
5.55e+01	
-4.22e+01	
-1.40e+02	
-2.38e+02	
-3.35e+02	
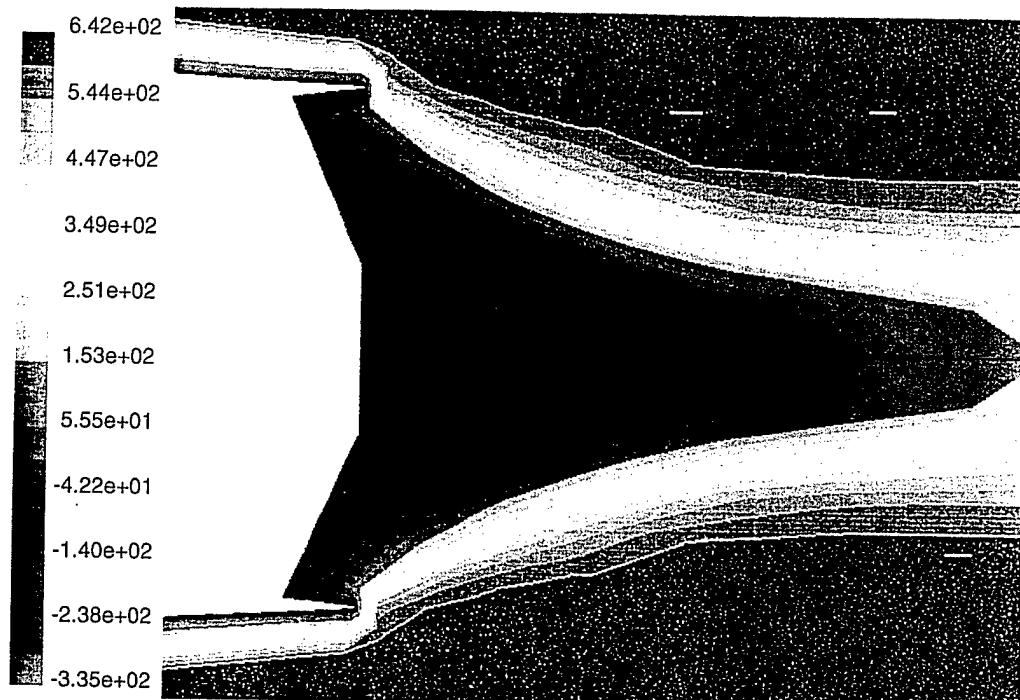
Mar 29, 2000
FLUENT 5.3 (axi, coupled imp, RSM)

Figure 37. Contours of axial mean velocity (zoom) for M = 3.0 with wake combustion.

1.93e+02	
1.55e+02	
1.18e+02	
8.08e+01	
4.35e+01	
6.17e+00	
-3.11e+01	
-6.85e+01	
-1.06e+02	
-1.43e+02	
-1.80e+02	
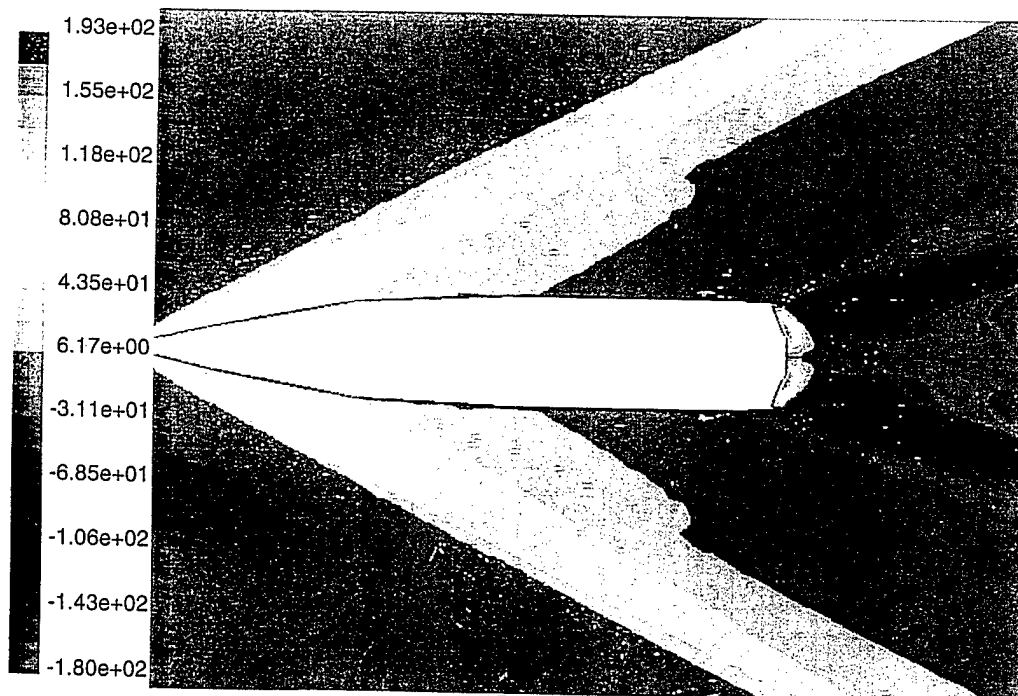
Mar 28, 2000
FLUENT 5.3 (axi, coupled imp, S-A)

Figure 38. Contours of radial mean velocity for M = 3.0 with wake combustion.

41

Table 1. Experimental flow conditions and geometry.

Flow Property and Geometry	Magnitude
Free Stream Static Pressure	28700 Pa
Approach Free Stream Mach Number	2.47
Tunnel Stagnation Temperature	300 K
Bleed Flow Mass Flow Rate Ratio	0.01
Base Radius	31.75 mm
Bleed Orifice Radius	12.7 mm
Bleed Flow Stagnation Temperature	300 K
Tunnel Stagnation Pressure	470000 Pa

Table 2. Turbulence closure models.

Tubulence Closure Models	Key Features/Assumptions
Spalart-Allmaras Model	Boussinesq approximation, 1-equation
Standard k-ε Model	Relates dissipation rate and turbulent kinetic energy, 2-equation
RSM	Relates Reynolds stresses and dissipation rate, 5-equation

Table 3. Turbulence closure models and cell density.

Turbulence Model	Coarse Density	Medium Density	Fine Density
Spalart-Allmaras	7197	15724	63809
k-ε	8770	15724	63809
RSM	8690	15724	63809

Table 4. Computational flow conditions for M549 projectile.

Flow Property and Geometry	Magnitude/Characteristic
Projectile	M549
Free Stream Static Pressure	28700 Pa
Approach Free Stream Mach Number	2.47
Tunnel Stagnation Temperature	300 K
Turbulence Model	RSM 5-equation
Cell Density	71234
Mass Base Bleed	NA
Tunnel Stagnation Pressure	470000 Pa

Table 5. Computational flow conditions for M864 projectile.

Flow Property and Geometry	M = 0.8		M = 1.5		M = 3.0	
Projectile	M864		M864		M864	
Free-Stream Static Pressure (Pascals)	28700		28700		28700	
Stagnation Temperature (Kelvin)	300		300		300	
Cell Density	105,500		105,500		105,500	
Stagnation Pressure (Pascals)	43738.8		105357.7		1054237	
Turbulence Model (RSM/5-equation)	RSM	5-eq	RSM	5-eq	RSM	5-eq
Mass Base Bleed (I)	0.01	0.01	0.01	0.01	0.01	0.01
Wake Combustion (No/Yes)	N	Y	N	Y	N	Y

INTENTIONALLY LEFT BLANK.

6. References

1. Fluent, Inc. *FLUENT*. Version 5.1.1, Lebanon, NH, 1999.

2. Sahu, J. "Numerical Computations of Supersonic Base Flow with Special Emphasis on Turbulence Modeling." *American Institute of Aeronautics and Astronautics Journal*, vol. 32, no. 7, pp. 1547–1549.

3. Sahu, J., and K. Heavey. "Computational Study of Base Bleed Flow and Comparison With Experimental Data." 16th International Symposium on Ballistics, San Francisco, CA, 23–28 September 1996.

4. Sturek, W. B., C. J. Nietubicz, J. Sahu, and P. Weinacht. "Recent Applications of CFD to the Aerodynamics of Army Projectiles at the U.S. Army Ballistic Research Laboratory." ARL-TR-22, U.S. Army Research Laboratory, Aberdeen Proving Ground, MD, December 1992.

5. Dutton, J. C., and A. L. Addy. "Fluid Dynamic Mechanisms and Interactions Within Separated Flows." U.S. Army Research Office Research Grant DAAH04-93-G-0226 and the Department of Mechanical and Industrial Engineering, University of Illinois, Urbana-Champagne, Urbana, IL, August 1998.

6. Fluent, Inc. "Gambit Training Notes." TRN-1998-003, Lebanon, NH, December 1998.

7. Herrin, J. L., and J. C. Dutton. "Effects of Afterbody Boattailing on the Near-Wake of Axisymmetric Bodies in Supersonic Flow." AIAA94-0029, 32nd Aerospace Sciences Meeting and Exhibit, Reno, NV, 10–13 January 1994.

8. Reid, J., and R. C. Hastings. "Experiments on the Axisymmetric Flow Over Afterbodies and Bases at M = 2.0." RAE Report Aero 2628, Royal Aircraft Establishment, Farnborough, England, 1959.

9. Fluent, Inc. "Fluent5 Solver Training Notes Day 1 and 2." TRN-1998-006, Lebanon, NH, 31 December 1998.

10. Nietubicz, C. J., and H. J. Gibeling. "Navier Stokes Computations for a Reacting, M864 Base Bleed Projectile." ARL-TR-875, U.S. Army Research Laboratory, Aberdeen Proving Ground, MD, 1995.

11. Giebling, H. J., and R. C. Buggeln. "Reacting Flow Models for Navier-Stokes Analysis of Projectile Base Combustion." AIAA Paper 91-2077, American Institute of Aeronautics and Astronautics, Reston, VA, June 1991.

INTENTIONALLY LEFT BLANK.

NO. OF COPIES	ORGANIZATION
2	DEFENSE TECHNICAL INFORMATION CENTER DTIC OCA 8725 JOHN J KINGMAN RD STE 0944 FT BELVOIR VA 22060-6218
1	HQDA DAMO FDT 400 ARMY PENTAGON WASHINGTON DC 20310-0460
1	OSD OUSD(A&T)/ODDR&E(R) DR R J TREW 3800 DEFENSE PENTAGON WASHINGTON DC 20301-3800
1	COMMANDING GENERAL US ARMY MATERIEL CMD AMCRDA TF 5001 EISENHOWER AVE ALEXANDRIA VA 22333-0001
1	INST FOR ADVNCD TCHNLGY THE UNIV OF TEXAS AT AUSTIN 3925 W BRAKER LN STE 400 AUSTIN TX 78759-5316
1	US MILITARY ACADEMY MATH SCI CTR EXCELLENCE MADN MATH THAYER HALL WEST POINT NY 10996-1786
1	DIRECTOR US ARMY RESEARCH LAB AMSRL D DR D SMITH 2800 POWDER MILL RD ADELPHI MD 20783-1197
1	DIRECTOR US ARMY RESEARCH LAB AMSRL CI AI R 2800 POWDER MILL RD ADELPHI MD 20783-1197

NO. OF COPIES	ORGANIZATION
3	DIRECTOR US ARMY RESEARCH LAB AMSRL CI LL 2800 POWDER MILL RD ADELPHI MD 20783-1197
3	DIRECTOR US ARMY RESEARCH LAB AMSRL CI IS T 2800 POWDER MILL RD ADELPHI MD 20783-1197

ABERDEEN PROVING GROUND

2	DIR USARL AMSRL CI LP (BLDG 305)

NO. OF
COPIES   ORGANIZATION

1   UIUC
     DEPT OF MECHL AND
     INDUSTRIAL ENGRG
     J C DUTTON
     URBANA IL 61801

1   D J HAROLDSEN
     1008 JOHNSVILLE ROAD
     ELDERSBURG MD 21784

1   DIR DIV OF ENGRG DESIGN
     G C CATALANO
     THE WATSON SCHOOL
     SUNY AT BINGHAMTON
     PO BOX 6000
     BINGHAMTON NY 13902-6000

1   TETRA RESEARCH CORP
     R CHAMBERLAIN
     2610 SPICEWOOD TR
     HUNTSVILLE AL 35811-2604

1   RICE MEMS
     M BEHR
     MS 321
     6100 MAIN ST
     HOUSTON TX 77005

1   FLUENT INCORPORATED
     DR A LYTLE
     10 CAVENDISH CT
     CENTERRA RESEARCH PK
     LEBANON NH 03766

     ABERDEEN PROVING GROUND

9   AMSRL WM BC
        P PLOSTINS
        B GUIDOS
        K HEAVEY
        J SAHU
        P WEINACHT
        J DESPIRITO
     AMSRL CI H
        C NIETUBICZ
        A MARK
        D PRESSEL

48

REPORT DOCUMENTATION PAGE

Public reporting burden for this collection of information is estimated to average 1 hour per response, including the time for reviewing instructions, searching existing data sources, gathering and maintaining the data needed, and completing and reviewing the collection of information. Send comments regarding this burden estimate or any other aspect of this collection of information, including suggestions for reducing this burden, to Washington Headquarters Services, Directorate for Information Operations and Reports, 1215 Jefferson Davis Highway, Suite 1204, Arlington, VA 22202-4302, and to the Office of Management and Budget, Paperwork Reduction Project(0704-0188), Washington, DC 20503.

1. AGENCY USE ONLY (Leave blank)	2. REPORT DATE	3. REPORT TYPE AND DATES COVERED
	September 2001	Final, January 1999 – July 2000

4. TITLE AND SUBTITLE	5. FUNDING NUMBERS
A Numerical Investigation of Subsonic and Supersonic Flow Around Axisymmetric Bodies	423612.000

6. AUTHOR(S)

George D. Catalano* and Walter B. Sturek, Sr.

7. PERFORMING ORGANIZATION NAME(S) AND ADDRESS(ES)	8. PERFORMING ORGANIZATION REPORT NUMBER
U.S. Army Research Laboratory ATTN: AMSRL-CI-HA Aberdeen Proving Ground, MD 21005-5067	ARL-TR-2595

9. SPONSORING/MONITORING AGENCY NAMES(S) AND ADDRESS(ES)	10. SPONSORING/MONITORING AGENCY REPORT NUMBER

11. SUPPLEMENTARY NOTES

*U.S. Military Academy, Department of Civil and Mechanical Engineering, West Point, NY 10996.

12a. DISTRIBUTION/AVAILABILITY STATEMENT	12b. DISTRIBUTION CODE
Approved for public release; distribution is unlimited.	

13. ABSTRACT(Maximum 200 words)

A computational fluid dynamics (CFD) approach to predicting high-speed aerodynamic flow fields of interest to the U.S. Army Research Laboratory (ARL) has been carried out. The aerodynamic problems of particular interest are (1) supersonic flow past the aftbody of projectiles with base mass injection, (2) supersonic flow past the M549 projectile, and (3) subsonic, transonic, and supersonic flow past an M864 projectile with base bleed and wake combustion.

The commercially available FLUENT (Fluent, Inc. *FLUENT*. Version 5.1.1, Lebanon, NH, 1999.) CFD code was utilized. The computational effort supports an ongoing ARL-sponsored experimental investigation. Of particular interest in the present investigation is the careful characterization of the various turbulence models employed in the CFD code. Additionally, the ease of use and set-up as well as the computational time will be described.

An experimental effort (Dutton, J. C., and A. L. Addy. "Fluid Dynamic Mechanisms and Interactions Within Separated Flows." U.S. Army Research Office Research Grant DAAH04-93-G-0226 and the Department of Mechanical and Industrial Engineering, University of Illinois, Urbana-Champagne, Urbana, IL, August 1998.) consisting of detailed laser Doppler velocimeter (LDV), particle image velocimeter (PIV), and high-speed wall pressure measurements has been made in axisymmetric and planar subsonic and supersonic flows with embedded separated regions. The present work seeks to predict similar flow fields computationally and to address areas of agreement and disagreement.

14. SUBJECT TERMS		15. NUMBER OF PAGES
computational fluid dynamics, supersonic base flow, turbulence modeling, projectile aerodynamics		53
		16. PRICE CODE

17. SECURITY CLASSIFICATION OF REPORT	18. SECURITY CLASSIFICATION OF THIS PAGE	19. SECURITY CLASSIFICATION OF ABSTRACT	20. LIMITATION OF ABSTRACT
UNCLASSIFIED	UNCLASSIFIED	UNCLASSIFIED	UL

INTENTIONALLY LEFT BLANK.